Desalination and Water Treatment
www.deswater.com
doi: 10.5004/dwt.2021.26971

218 (2021) 309–326
April

Efficient removal of Pb(II) with manganese oxide modified from low grade pyrolusite

Yujue Zhang[a], Luhua Kang[a,b], Peng Zhu[a], Shijun Su[a], Sanglan Ding[a], Weiyi Sun[a,*], Zhenfeng Cai[b]

[a]*College of Architecture and Environment, Sichuan University, Chengdu 610065, China, Tel. +13458583411; email: swylsculw@163.com (W. Sun), Tel. +13547984683; email: 1152788039@qq.com (Y. Zhang), Tel. +19970097805; email: klhscu@163.com (L. Kang), Tel. +18224451058; email: 1332159399@qq.com (P. Zhu), Tel. +13980676135; email: ssjscu@163.com (S. Su), Tel. +18602888389; email: dslscu@163.com (S. Ding)*
[b]*Jiangxi Huagan Environmental Technology Development Co., Ltd., Nanchang 330096, China, Tel. +18779881702; email: chfhl@163.com*

Received 30 May 2020; Accepted 25 December 2020

ABSTRACT

In this paper, the manganese oxide (HMO) modified from low-grade pyrolusite by the NaOH molten roasting and washing processes was used as a low-cost and efficient adsorbent for toxic metal removal. The HMO showed excellent selective sorption and regeneration for Pb^{2+}. Furthermore, the equilibrium adsorption isotherm was well-fitted by Langmuir models. The adsorption process was described by the pseudo-secondary kinetics. Characterization results of X-ray diffraction, energy-dispersive X-ray spectroscopy, infrared, and X-ray photoelectron spectroscopy showed that Pb^{2+} adsorption by HMO mainly depended on complexation reaction between hydroxyl groups on the surface and Pb^{2+} from aqueous solution.

Keywords: Manganese oxide adsorbent; Low-grade pyrolusite; Pb^{2+} adsorption; Adsorption kinetics; Adsorption isotherm; Thermodynamics

1. Introduction

Lead (Pb^{2+}) is one of the most toxic metals, which can cause damage to the kidney and blood vessel blockage [1,2]. Because of the seriousness of Pb^{2+} pollution, lots of methods were adopted to remove Pb^{2+} from wastewater, such as physicochemical method-redox [3,4], adsorption [5,6], filtration [7–10], etc. Among these methods, adsorption is usually used because of its high efficiency and easy application [11,12]. Commonly used Pb^{2+} adsorption materials included clay [13], activated carbon [14], resin [15], alumina [16], carbon nanorods [17], magnetite [18], and manganese oxide (HMO) [19].

HMO has proven to be an efficient absorbent for Pb^{2+} removal [20], because the surface of HMO adsorbent is rich in hydroxyl group with porous structure and large specific surface area [21,22]. Currently, HMO is prepared by the high-purity manganese salts, such as $MnSO_4$ and $KMnO_4$, via synthetic methods of hydrothermal method [20], sol–gel method [23–25], chemical oxidation method [26,27], and so on. It could be noted, high-purity manganese salts used for adsorbent production are obtained from manganese ores through processes of leaching, purifying, pyrolysis, and recovery. Tedious preparation processes of manganese salts increase the cost of HMO adsorbent. Therefore, replacing high-purity manganese salts and setting sights on cheap raw materials for Pb^{2+} adsorbent production is an important issue needed to be solved.

China has a rich reserve of low-grade pyrolusite (Mn content < 30%), which is an important manganese ore for manganese salts production. Although MnO_2, which is the existence form of Mn in pyrolusite, is confirmed as an

* Corresponding author.

efficient Pb^{2+} absorbent according to existing researches, the low-grade pyrolusite cannot be used as Pb^{2+} absorbent directly due to the low Mn content and lack of adsorption activity. Therefore, using relatively simple methods to modify low-grade pyrolusite to increase Pb^{2+} adsorption capacity is very significative for cost-effective Pb^{2+} adsorbent production.

In this paper, low-grade pyrolusite was treated by the pyrolusite–NaOH molten roasting and washing processes to remove Si, Al, and Fe, obtaining the HMO adsorbent with good channel structure, higher Mn content, and larger Pb^{2+} adsorption capacity. Roasting atmosphere, roasting temperature, NaOH–pyrolusite ratio, and roasting time in the roasting process and HCl concentration in preparing process were investigated, at the same time, the experiments of influential factors on Pb^{2+} adsorption progress, adsorption kinetics, adsorption apparent activation energy, adsorption isotherm, and thermodynamics, etc., demonstrated excellent Pb^{2+} sequestration of HMO. Mechanisms of adsorbent preparation and Pb^{2+} adsorption were analyzed by characterizations of different adsorbent samples using X-ray diffraction (XRD), scanning electron microscopy (SEM), X-ray fluorescence (XRF), infrared (IR), X-ray photoelectron spectroscopy (XPS), and Brunauer–Emmett–Teller (BET). Finally, the relationship between Pb^{2+} adsorption amount and H^+ release amount in the adsorption process was explored.

2. Materials and methods

2.1. Materials

Low-grade pyrolusite (Guangxi, China) was ground and screened into 75 μm particle size. The chemical composition was shown in Table 1. As we could see, the Mn content in pyrolusite was 28.54%, and the content of the main impurities including Si, Fe, and Al were 19.07%, 3.10%, and 0.61%, respectively. Other impurities such as Ca, Zn, and Ni were less than 1.00%. XRD analysis (Fig. 1) indicated that Si in pyrolusite mainly presented in the form of silicon oxide, while Mn was existed primarily in amorphous manganese dioxide.

Other materials, including sodium hydrous (NaOH), lead nitrate ($Pb(NO_3)_2$), hydrochloric acid (HCl), sulfuric acid (H_2SO_4, 98%), nitric acid (HNO_3), and phosphoric acid (H_3PO_4) used in this study were of analytical grade.

2.2. Batch sorption experiments of HMO adsorbent

Actually, in roasting experiments, a specified amount of pyrolusite was homogeneously mixed with NaOH in a corundum crucible, and then heated at various temperatures (300°C–700°C) for a required time (60–300 min). Distilled water and HCl solution (1.0 mol/L) were used to wash the roasted sample at 50°C for 30 min, respectively. While the sample was washed to neutral with distilled water, at last, HMO was obtained after a drying process. During the washing and pickling process, the dissolution of Mn($Mn_{(loss)}$), was calculated using the following formula:

$$Mn_{(loss)} = \frac{c_1V_1 + c_2V_2}{mw \times 1{,}000} \times 100\% \quad (1)$$

where $Mn_{(Loss)}$ is the dissolution of Mn, (%); c_1 and c_2 are the Mn content of water washing and pickling solution, respectively, (mg/L); V_1 and V_2 are the volume of water washing and pickling solution, respectively, (L); m is the mass of roasting product, (g); w is the percentage of Mn in the roasting product, (%).

In the preparing process, the working Pb^{2+} solutions were freshly prepared using distilled water. 0.1 g HMO was added into 200 mL solution with Pb^{2+} concentration of 250 mg/L in thermostatic magnetic stirrer at 30°C, the pH was constantly kept at 5.0. Subsequently, the reacted solution was taken at different contact time (0.5, 1, 2, 5, 15, 30, 60, and 120 min) by syringe, analyzed for the Pb^{2+} concentration by inductively coupled plasma mass spectrometry (ICP-MS) which were filtered again through 0.22 μm syringe-driven filters. The adsorption capacity of HMO was calculated using the following formula:

$$Q = \frac{(c_0 - c_t)V}{m} \quad (2)$$

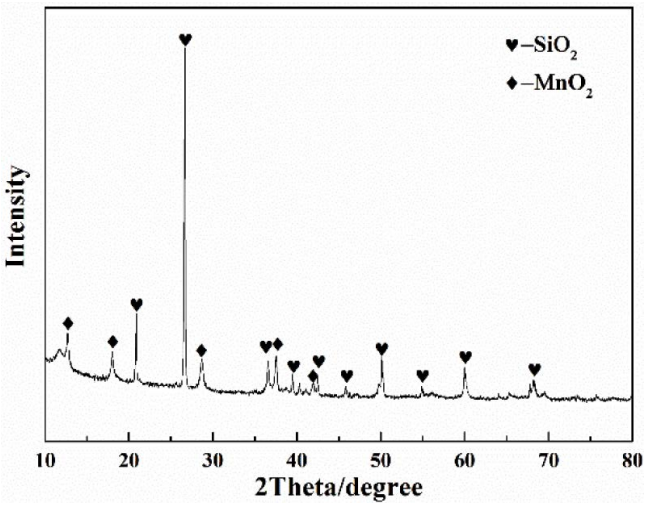

Fig. 1. X-ray diffraction pattern of pyrolusite.

Table 1
Element composition analysis of pyrolusite and HMO (wt.%)

	Mn	Si	Fe	Al	Ca	Zn	Ni	Ti
Pyrolusite	28.54	19.07	3.10	0.61	0.23	0.078	0.061	0.032
HMO	48.03	1.62	3.97	0.13	0.055	0.051	0.091	0.045

where Q is the adsorption capacity, mg/g, c_0 and c_t are the initial concentration and the concentration at time t, mg/L, respectively. V is the volume of solution, mL, and m is the mass of used adsorbent, g.

In the adsorption parameter experiments, the certain known volume of lead nitrate solution (124, 166, 208, 250, 292, 334, and 418 mg/L) was put into a beaker which was fixed on the constant temperature magnetic heating agitator at a certain speed. Then pH value (2.0, 3.0, 4.0, 5.0, and 6.0) was kept with 0.1 mol/L nitric acid or sodium hydroxide solution. Other factors such as contact time which was embodied by different time intervals and dosage of HMO (0.250, 0.375, 0.500, 0.625, 0.750, 0.875, and 1.000 g/L) were evaluated, too. During the adsorption process, the adsorption capacity was the same as Eq. (2) and removal rate of toxic metals were calculated by the following formula:

$$\eta = \frac{c_0 - c_t}{c_0} \times 100\% \tag{3}$$

where η is the removal rate of toxic metal, %, c_0 and c_t are the initial concentration of toxic metal and concentration at the time of t minutes of the toxic metal, respectively, mg/L.

2.3. Experiments of adsorption studies

The procedure of preparing lead nitrate solutions with different initial concentrations (124, 166, 208, 250, 292, 334, and 418 mg/L), ambient temperature (30°C, 40°C, 50°C, and 60°C), and initial pH values (2.0, 3.0, 4.0, 5.0, and 6.0) were same as the adsorption experiments in 2.2, and the HMO dosage was chosen as 0.625 g/L under 200 mL solution. Then immediately took samples at different time intervals (0.5, 1, 2, 5, 15, 30, and 60 min, respectively). During the adsorption process, the adsorption capacity and removal rate of toxic metals were calculated by Eqs. (2) and (3).

2.3.1. Adsorption isotherms

By fitting the adsorption data with different adsorption isotherm models, the relationship between adsorbents and adsorbates can be described, and the adsorption mechanism can be predicted [28,29]. The data were fitted into Langmuir and Freundlich isotherms [30,31].

2.3.1.1. Langmuir isotherm

This model assumes that all active sites on the adsorbent have only one corresponding adsorbed molecule. Once a molecule occupies an active site, other molecules can no longer occupy it, that is, the single-molecule adsorption model [32]. The model is applicable to physical and chemical adsorption, and the equation can be expressed as follows:

$$Q_e = Q_{\max} \frac{K_L c_e}{1 + K_L c_e} \tag{4}$$

The linear form is as follows:

$$\frac{c_e}{Q_e} = \frac{c_e}{Q_{\max}} + \frac{1}{K_L Q_{\max}} \tag{5}$$

where $Q_{\max}$ is the adsorption capacity on the surface of the adsorbent, mg/g, K_L is Langmuir adsorption equilibrium constant, L/mg, Q_e and c_e are equilibrium adsorption and equilibrium concentration, respectively, mg/g and mg/L.

2.3.1.2. Freundlich isotherm

This model indicates that the adsorbent surface has uneven adsorption sites, toxic metal ions are preferentially adsorbed to sites with higher activity, and adsorption heat decreases with the decrease numbers of adsorption sites. This model is also applicable to physical and chemical adsorption, and the equation can be expressed as follows:

$$Q_e = K_F c_e^{\frac{1}{n}} \tag{6}$$

The linear form is as follows:

$$\log Q_e = \log K_F + \frac{1}{n} \log C_e \tag{7}$$

where K_F is Freundlich adsorption equilibrium constant, L/g, n is the characteristic constant related to adsorption strength, Q_e and c_e are equilibrium adsorption and equilibrium concentration, respectively, mg/g and mg/L.

2.3.2. Kinetic studies

The common adsorption kinetics models include pseudo-first-order kinetics, pseudo-second-order kinetics, and particle internal diffusion model [33].

2.3.2.1. Pseudo-first-order kinetic model

$$\ln\left(Q_e - Q_t\right) = \ln Q_e - K_1 t \tag{8}$$

The linear form is as follows:

$$\log\left(Q_e - Q_t\right) = \log Q_e - \frac{K_1 t}{2.303} \tag{9}$$

where Q_e and Q_t are the equilibrium adsorption capacity and the adsorption capacity at the time of t minutes, respectively, mg/g, K_1 is the pseudo-first-order adsorption rate constant, min^{-1}, t is the time of adsorption, min.

2.3.2.2. Pseudo-second-order kinetic model

$$\frac{1}{Q_e - Q_t} = \frac{1}{Q_e} + K_2 t \tag{10}$$

The linear form is as follows:

$$\frac{t}{Q_t} = \frac{t}{Q_e} + \frac{1}{K_2 Q_e^2} \tag{11}$$

where Q_e and Q_t are the equilibrium adsorption capacity and the adsorption capacity at the time of t minutes, respectively,

mg/g, K_2 is the pseudo-second-order adsorption rate constant, min^{-1}, t is the time of adsorption, min.

2.3.2.3. Particle internal diffusion model

$$Q_t = K_3\sqrt{t} + C \tag{12}$$

where Q_t is the adsorption capacity at the time of t minutes, K_3 is the particle internal diffusion rate constant, mg/g $min^{0.5}$.

2.3.3. Thermodynamic studies

The Gibbs free energy change (ΔG), enthalpy (ΔH), and entropy change (ΔS) are used to describe spontaneity, adsorption heat, and degree of chaos system of adsorption process in the adsorption thermodynamics.

According to the laws of thermodynamics, the equation of the Gibbs free energy change is expressed as follows [34,35]:

$$\Delta G = -RT\ln K_d \tag{13}$$

The relationship between the Gibbs free energy change and the entropy change and the enthalpy change is as follows:

$$\Delta G = \Delta H - T\Delta S \tag{14}$$

Combining Eqs. (14) and (15) we can get the following equation:

$$\ln K_d = -\frac{\Delta H}{TR} + \frac{\Delta S}{R} \tag{15}$$

where K_d is the distribution coefficient, which can be obtained by the following formula:

$$K_d = \frac{Q_e}{c_e} \tag{16}$$

Combining Eqs. (4)–(16) and (4)–(17) we can get the following equation:

$$\ln\left(\frac{Q_e}{c_e}\right) = -\frac{\Delta H}{TR} + \frac{\Delta S}{R} \tag{17}$$

where R is the air constant, 8.314 J/mol/K; T is adsorption temperature, K; K_d is distribution constant, mL/g; Q_e is adsorption equilibrium capacity, mg/g; c_e is the equilibrium concentration, mg/L.

Activation energy of the adsorption process can be derived by fitting the Arrhennius formula and kinetic adsorption rate constant K:

$$\ln K = -\frac{E_a}{RT} + \ln A \tag{18}$$

where E_a is the apparent activation energy, kJ/mol; A is and pre-finger factor; R is the air constant, 8.314 J/mol/K; T is adsorption temperature, K.

2.4. Experiments of adsorption mechanism exploring

The procedure of preparing lead nitrate solutions with different initial concentrations, ambient temperature, and initial pH value were same as 2.3. At the adsorption time of 60 min, the mixture of HMO and lead nitrate solution was extracted and separated, and the filtered solution was reclaimed. The labeled sodium hydroxide solution was used to titrate the filtrate until the endpoint of pH value of the titration kept stable at 5.0, and the amount of sodium hydroxide solution in the titration process was recorded to calculate the release molar of hydrogen ion and the adsorption mole numbers of lead ion in the adsorption process. The release mole of hydrogen ion and the adsorption mole of lead ion in the adsorption process were fitted linearly according to the following formulas:

$$n_{\mathrm{Pb}} = \left(c_3 - c_4\right) \times V_3 \tag{19}$$

$$n_{\mathrm{H}} = \frac{c_5\left(V_4 - V_5\right)}{1{,}000} \tag{20}$$

where c_3 and c_4 are initial concentration and equilibrium concentration of Pb^{2+}, respectively, mg/L, c_5 is sodium hydroxide solution concentration, mg/L, V_3 is the volume of the reaction solution, L, V_4 and V_5 are readings of the basic burets before and after titration respectively, L.

2.5. Experiments of competitive adsorption

Competitive adsorption experiments were divided into two parts: (1) lead nitrate solution, copper nitrate solution, cadmium nitrate solution, cobalt nitrate solution, and nickel nitrate solution of 250 mg/L were prepared to separately react with HMO. And then according to the experimental method of adsorption experiment mentioned in 2.3, measured the concentration of toxic metal ions before and after adsorption and calculated the equilibrium adsorption capacity when experiments were reached adsorption equilibrium. (2) Lead nitrate solution, copper nitrate solution, cadmium nitrate solution, cobalt nitrate solution, and nickel nitrate solution of 250 mg/L were prepared to jointly react with HMO. Then according to the experimental method of adsorption experiment mentioned in 2.3, calculated the equilibrium adsorption capacity of metal ions respectively when the experiment was reached adsorption equilibrium.

2.6. Experiments of resorption

The adsorbent after sequestrating cations (PbMO) was put into 2 M nitric acid solution to desorb Pb^{2+} at a fixed time interval (120 min). Finally, PbMO was washed with deionized water to neutral, dried, and used for resorption. The desorption rate formula is as follows:

$$\tau = \frac{c_r V_7}{\left(c_0 - c_1\right) \times V_6} \times 100\% \tag{21}$$

where c_0 and c_1 are the initial concentration of toxic metal and equilibrium concentration of toxic metal in adsorption experiment, respectively, mg/L; c_r is the concentration of

toxic metal in resorption experiment, mg/L; V_1 and V_2 are adsorption and desorption solution volumes, respectively, mL; τ is Pb^{2+} desorption rate, %.

2.7. Characterization

Samples that needed to be characterized included pyrolusite, adsorbents before (HMO), and after adsorption of Pb^{2+} (PbMO). The crystalline phases of samples were characterized by XRD (EMPYREAN, Panalytical Co., Ltd., Almelo, The Netherlands) using graphite monochromatized Cu Ka radiation (k = 1.54056 Å). The chemical composition and crystal morphology of samples were analyzed by XRF (XRF-1800) and SEM (JSM-7500F, JEOL Ltd., Tokyo, Japan). The specific surface areas and chemical bonds of samples were analyzed by the BET method (AUTOSORB-IQ) and Fourier transforms infrared (FTIR) spectrometer (Nicolet 6700), respectively. The samples were qualitatively and semi-quantitatively analyzed by electron beam interaction with solid microregions on SEM (JSM-7500F). And XPS (XSAM800, Kratos, UK) was used to analyze changes in the valence and content of elements on the surface before and after adsorption.

3. Results and discussion

3.1. Preparation parameters of HMO

3.1.1. Effect of roasting atmosphere

Under the condition of 400°C, NaOH–pyrolusite ratio at 1:1, roasting time of 120 min, the roasting results under N_2 and air conditions were compared to investigate the effect of oxygen on the roasting process, and comparison of roasting in air and N_2 are shown in Fig. 2.

It can be concluded that the presence of O_2 had an important effect on the roasting process. Compared with the roasting results in air, roasting in the N_2 atmosphere could lower the Mn dissolution and achieve higher Pb^{2+} absorption capacity and Mn content in the HMO. The reason was that MnO_2 could be converted into Na_2MnO_4 [36]. Under the condition of the coexistence of NaOH and O_2 through the chemical reaction (22), and then dissolved in the washing solution in the washing process. Therefore, in order to reduce the Mn dissolution and improve the Pb^{2+} adsorption capacity, the roasting process should be carried out in the N_2 atmosphere.

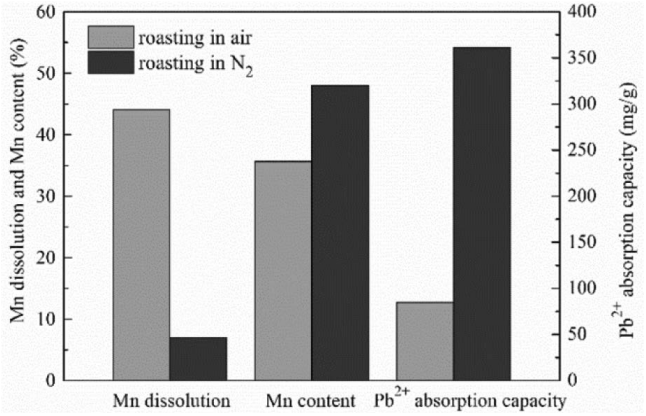

Fig. 2. Comparison of roasting in air and roasting in N_2 (reaction temperature: 400°C; NaOH–pyrolusite ratio at 1:1; roasting time: 120 min).

$$2MnO_2(s) + 4NaOH(s) + O_2(g) = 2Na_2MnO_4(s) + 2H_2O(g) \quad (22)$$

3.1.2. Effect of roasting temperature

Fig. 3 shows the effect of roasting temperature on Mn content in adsorbent, Mn dissolution, and Pb^{2+} adsorption capacity under the condition of NaOH–pyrolusite ratio at 1:1, roasting time of 120 min.

The curves in Fig. 3a indicate that the Mn dissolution increased dramatically when roasting temperature increased, and Mn content in HMO decreased slowly at the same time. With the increasing of roasting temperature from 400°C to 700°C, the Mn dissolution increased from 6.96% to 27.23%, while the Mn content in HMO decreased from 48.03% to 46.59%. The reason for these changes was that high roasting temperature promoted the conversion of MnO_2 to Mn_2O_3 [37–39]. In the washing process, Mn_2O_3 reacted with HCl to produce MnO_2 and Mn^{2+}, and the extraction of Mn^{2+} leads to the increasing Mn dissolution and decreasing Mn content in HMO.

Fig. 3b indicates that Pb^{2+} adsorption capacity was improved with the increasing contact time, and finally reached equilibrium. As the heating temperature increased from 300°C to 400°C, Pb^{2+} adsorption capacity dramatically increased from 267.7 to 361.1 mg/g, however, with the further increase of the temperature from 400°C to 700°C, the Pb^{2+} adsorption capacity decreased. As the major component of adsorbent, the decrease of Mn content was one of the most important factors which caused a decrease of Pb^{2+} adsorption capacity. In addition, BET surface area of adsorbent was also an important factor, and highly effective adsorbents typically have a high surface area. Lots of investigations indicated that BET surface area of manganese-based functional materials can be effectively increased by the proper increase of roasting temperature [40], however, further increase of temperature could cause the adsorbents to harden, resulting in the drastic decreases of BET surface area and pore volume, which would affect their adsorption capability [38–43].

3.1.3. Effect of NaOH–pyrolusite ratio

The effect of NaOH–pyrolusite ratio on Pb^{2+} adsorption capacity, Mn dissolution, and Mn content were studied under the condition of 400°C, roasting time of 120 min.

Fig. 4a shows that the Mn content in adsorbent increased from 28.54% to 48.03% with increasing NaOH–pyrolusite ratio from 0:1 to 1:1, and then became immobile nearly. The change of Mn dissolution was almost independent on NaOH–pyrolusite ratio. Increasing of NaOH–pyrolusite ratio accelerated the reaction between NaOH and other metal oxides in pyrolusite, forming water-soluble, and acid-soluble production which were removed in the washing process, then indirectly increased Mn content in the adsorbent.

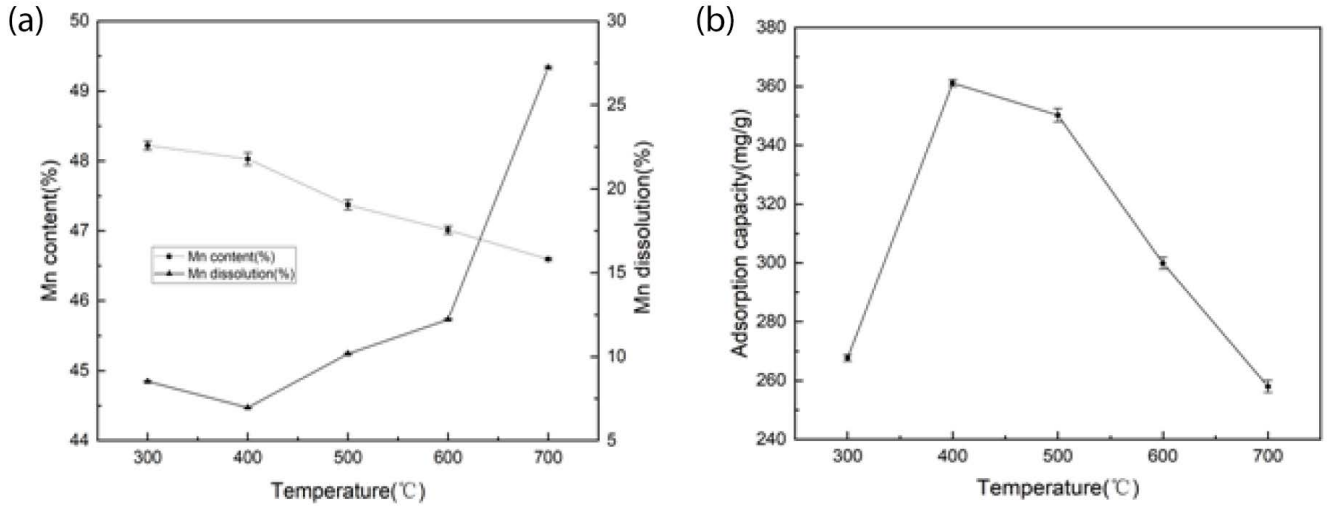

Fig. 3. Effect of roasting temperature on (a) Mn content and Mn dissolution (NaOH–pyrolusite ratio: 1:1; roasting time: 120 min) and (b) adsorption capacity of lead ($Pb(NO_3)_2$ concentration: 250 mg/L; HMO dosage: 0.5 g/L; reaction temperature: 30°C; pH: 5.0).

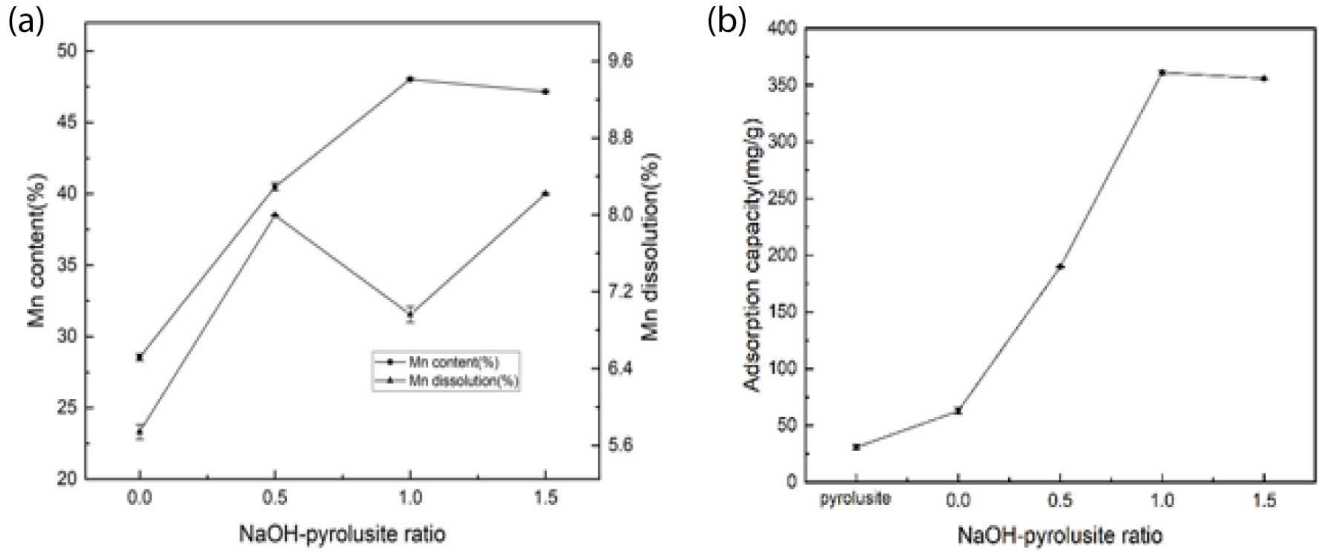

Fig. 4. Effect of NaOH–pyrolusite ratio on (a) Mn content and Mn dissolution (reaction temperature: 400°C; roasting time: 120 min) and (b) adsorption capacity of lead ($Pb(NO_3)_2$ concentration: 250 mg/L; HMO dosage: 0.5 g/L; reaction temperature: 30°C; pH: 5.0).

According to the experimental results given in Fig. 4b, compared with pyrolusite, the equilibrium Pb^{2+} adsorption capacity on HMO (NaOH–pyrolusite ratio = 0:1) was increased from 30.9 to 62.8 mg/g. In addition, the Pb^{2+} adsorption capacity on HMO modified by NaOH increased from 189.8 to 361.1 mg/g with increasing NaOH–pyrolusite ratio from 0.5:1 to 1:1. Upon a higher NaOH–pyrolusite ratio to 1.5, Pb^{2+} adsorption capacity did not further increase.

3.1.4. Effect of roasting time

Effects of roasting time on Pb^{2+} adsorption capacity, Mn dissolution, and Mn content were investigated under the condition of 400°C, NaOH–pyrolusite ratio of 1:1.

Fig. 5a indicates that Mn dissolution and Mn content were hardly affected by the roasting time. Moreover, the maximum Pb^{2+} equilibrium adsorption capacity of HMO in certain Pb^{2+} simulated wastewater was obtained at the roasting time of 120 min. This phenomenon was consistent with reported papers [44], and it could be easily explained that to form a sufficient number of micropores and mesopores was difficult due to the short roasting time which caused the inadequate reaction, however, if the roasting time was too long, the micropore structure formed before would be sintered and BET surface area would be reduced, resulting in the material performance degradation. Considering energy consumption, economic cost, and preparation effect, the most optimal condition of roasting time was 120 min.

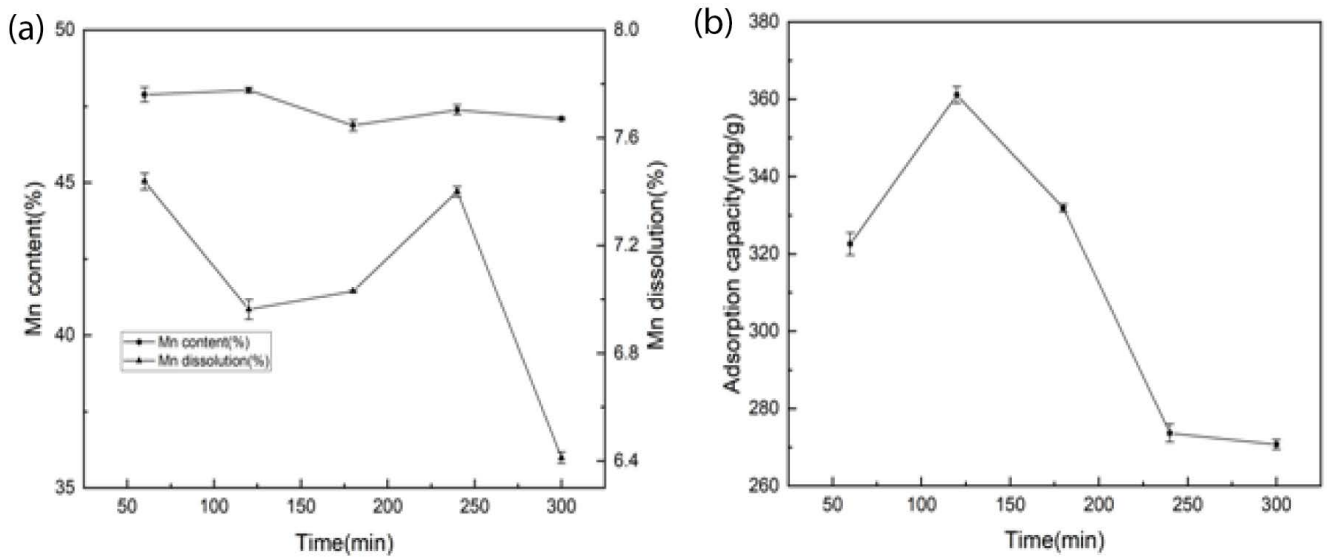

Fig. 5. Effect of (a) roasting time on Mn content and Mn dissolution (reaction temperature: 400°C; NaOH–pyrolusite ratio: 1:1) and (b) roasting temperature and time on adsorption capacity of lead ($Pb(NO_3)_2$ concentration: 250 mg/L; HMO dosage: 0.5 g/L; reaction temperature: 30°C; pH: 5.0).

In conclusion, the results showed that the Pb^{2+} adsorption capacity of HMO was 361.1 mg/g, the loss rate of manganese was 6.96%, and the content of manganese in the adsorbent was 48.03% under the conditions of 400°C calcination, 1:1 NaOH-pyrolusite ratio, and 120 min calcination time.

3.2. Effect of parameters on the adsorption process

3.2.1. Effect of HMO dosage

The effect of dosage on adsorption capacity by varying the quality of HMO from 0.250 to 1.000 g/L is shown in Fig. 6. Under the determined dosage, Pb^{2+} adsorption capacity of HMO increased with the increase of time and then tended to be flat. When the dosage was less than 0.625 g/L, Pb^{2+} adsorption capacity showed no significant decrease and when the dosage was more than 0.625 g/L, Pb^{2+} adsorption capacity began to decline in a straight line and ranged from 332.5 to 263.0 mg/g. That was because when the dosage was less than 0.625 g/L, the amount of Pb^{2+} in the solution was excessive compared with the total adsorption sites of HMO, and the adsorption sites are fully utilized. However, when the adding amount was more than 0.625 g/L, the total adsorption sites increased with the increasing of dosage, and the adsorbent surface had different strength of adsorption sites, resulting in competition of adsorption sites. The adsorption sites on HMO was not fully utilized, and the adsorption capacity also accordingly decreased. As for Pb^{2+} removal rate, it increased with the increase of HMO dosage. The main reason was that with the increase of dosage, the total number of adsorption sites on the adsorbent surface increased, while the amount of Pb^{2+} in the solution was invariable, so the removal rate accordingly increased. Therefore, in order to make full use of the adsorption sites with different strengths on the surface of HMO and to guarantee a certain amount of Pb^{2+} adsorption, the optimal dosage of this experiment was 0.625 g/L.

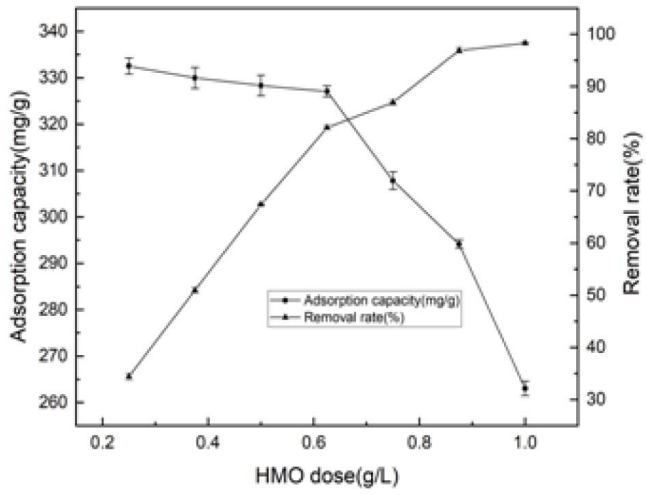

Fig. 6. Effect of dose on adsorption capacity and removal percentage of lead ($Pb(NO_3)_2$ concentration: 250 mg/L; reaction temperature: 30°C; pH: 5.0).

3.2.2. Effect of pH

Fig. 7 shows that Pb^{2+} adsorption capacity of HMO increased with time increasing at pH 2.0 to 6.0. The higher the pH value was, the higher Pb^{2+} adsorption capacity were.

According to Table 2 [45], hydrated ions formed by Pb^{2+} mainly existed in the form of $PbOH^+$. The selection of pH was to avoid hydrolysis of Pb^{2+}. When pH was 5.0, $PbOH^+$ in the solution accounted for 0.195% of total lead ions. When pH was 6.0, $PbOH^+$ accounted for 1.95% of

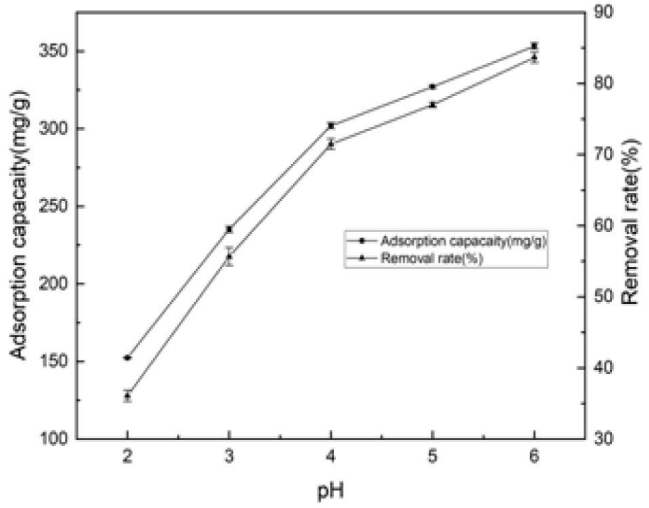

Fig. 7. Effect of pH on adsorption capacity and removal percentage of lead ($Pb(NO_3)_2$ concentration: 250 mg/L; HMO dosage: 0.625 g/L; reaction temperature: 30°C).

Table 2
Hydrolysis equilibrium and hydrolysis constant of Pb(II) in aqueous solution

Hydrolysis equilibrium equation	Hydrolysis constant
$Pb^{2+} + H_2O = PbOH^+ + 2H^+$	$K = 10^{-7.71}$
$Pb^{2+} + 2H_2O = Pb(OH)_{2(aq)} + 2H^+$	$K = 10^{-17.12}$
$Pb^{2+} + 3H_2O = Pb(OH)_3^- + 3H^+$	$K = 10^{-28.06}$
$Pb^{2+} + 4H_2O = Pb(OH)_4^{2-} + 4H^+$	$K = 10^{-40.8}$
$2Pb^{2+} + H_2O = Pb_2(OH)^{3+} + H^+$	$K = 10^{-6.36}$

total lead ions. Therefore, the pH value in the solution was kept at 5.0.

3.2.3. Effect of temperature and time

Fig. 8 shows the influence of time and temperature on Pb^{2+} sequestration. There was no doubt that the adsorption capacity increases with the increase of temperature. Furthermore, in the first 15 min, Pb^{2+} adsorption capacity of HMO increased rapidly, and then increased slowly with time lapsing until the reaction reached adsorption equilibrium. Therefore, the optimal adsorption time were controlled at 60 min.

3.2.4. Effect of initial Pb^{2+} concentration

We set Pb^{2+} initial concentration as 124, 166, 208, 250, 292, 334, and 418 mg/L. The effect of initial Pb^{2+} concentration on adsorption process was further investigated in Fig. 9. When Pb^{2+} concentration was 124 mg/L, the removal rate of Pb^{2+} was close to 100%, indicating that Pb^{2+} in the solution was almost completely adsorbed. With the increase of the initial concentration, Pb^{2+} adsorption capacity increased, however, Pb^{2+} removal rate decreased. When the concentration reached 292 mg/L, Pb^{2+} adsorption increased slowly until the reaction reached adsorption equilibrium.

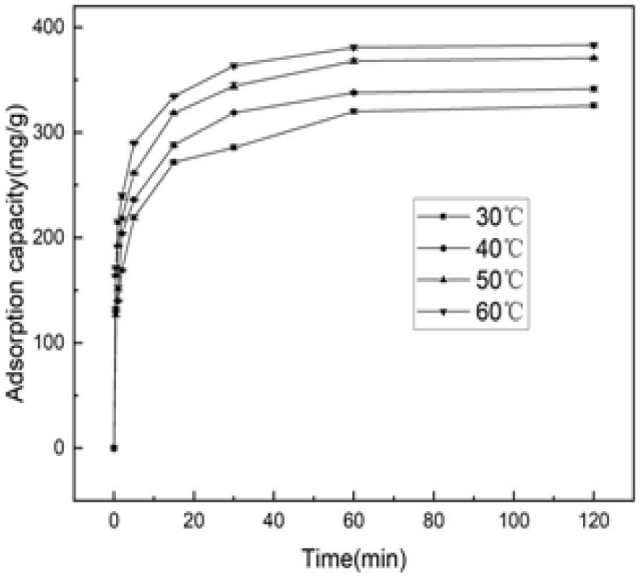

Fig. 8. Effect of time and temperature on adsorption capacity of lead ($Pb(NO_3)_2$ concentration: 250 mg/L; HMO dosage: 0.625 g/L; pH: 5.0).

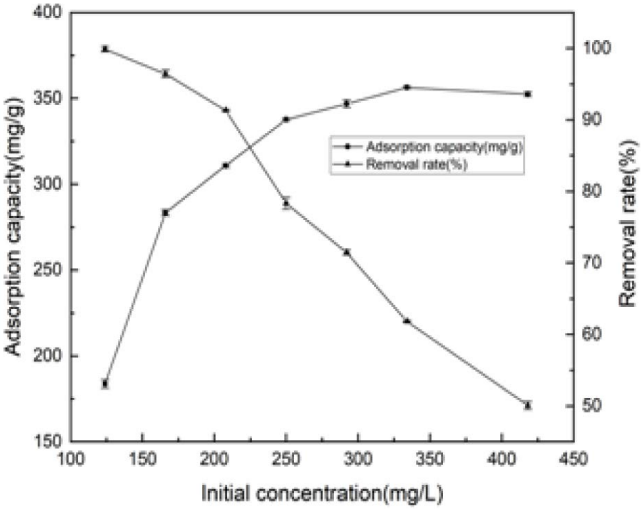

Fig. 9. Effect of initial concentration on adsorption capacity of lead (HMO dosage: 0.625 g/L; pH: 5.0; adsorption time: 60 min; Pb^{2+} initial concentration: 124, 166, 208, 250, 292, 334, and 418 mg/L).

In a word, the optimal adsorption experiment conditions were selected as 0.625 g/L of HMO, initial concentration of Pb^{2+} of 292 mg/L, pH value of 5.0, and adsorption time of 60 min. Furthermore, the adsorbed equilibrium amount of 395.0 mg/g was obtained under the conditions (when the reaction temperature reached 60°C).

3.3. Thermodynamic study of HMO

3.3.1. Adsorption isotherms

In order to explore Pb^{2+} adsorption performance and characteristics of HMO, the experimental readings at

different temperatures were fitted into Langmuir isotherm equation mentioned above (Fig. 10). Table 3 shows the determination coefficient R^2 of Langmuir isotherm was above 0.999 and the determination coefficient R^2 of Freundlich adsorption isotherm was less than 0.960, which indicated that the results fitted well in Langmuir isotherm. Moreover, the equilibrium adsorption capacity calculated by Langmuir equation was almost in accordance with experimental readings, demonstrating that Pb^{2+} adsorption process belonged to monolayer adsorption.

In this paper, the values of dimensionless equilibrium constant R_L were calculated and the formula was as follows:

$$R_L = \frac{1}{1 + K_L c_0} \tag{23}$$

where c_0 was the maximum initial concentration of toxic metal ions, mg/L, K_L was Langmuir adsorption equilibrium constant, L/mg.

It could be found from Table 4 that R_L in Langmuir equation was related to Pb^{2+} initial concentration. Under different initial concentration and temperature, values of R_L were far less than 1, illustrating that HMO was effective for Pb^{2+} adsorption.

3.3.2. Adsorption thermodynamics

The sorption of Pb^{2+} on HMO at 304, 314, 324, and 334 K was investigated. Results of linear fitting of $\ln(Q_e/c_e)$ vs. $(1/T)$ are shown in Fig. 11 and thermodynamic parameters are obtained in Table 5.

It can be seen from Table 6 that the negative values of ΔG at different temperatures indicated the spontaneous nature of the adsorption process. The positive values of ΔH in this adsorption process indicated the endothermic nature of the process. In addition, the positive values of entropy change ΔS attributed to structural changes and high affinity of Pb^{2+} of HMO [46].

3.4. Kinetics study of Pb^{2+} on the surface of HMO

3.4.1. Adsorption kinetics

The fitting results are shown in Fig. 12, and the obtained dynamic parameters and determination coefficients are shown in Table 6. As can be seen from Fig. 12, by applying the pseudo-second-order kinetic model a straight line was obtained. It was observed that R^2 of pseudo-second-order dynamics from Table 6 was all above 0.996, and the adsorption saturation (Q_e) calculated by fitting pseudo-second-order dynamics agreed

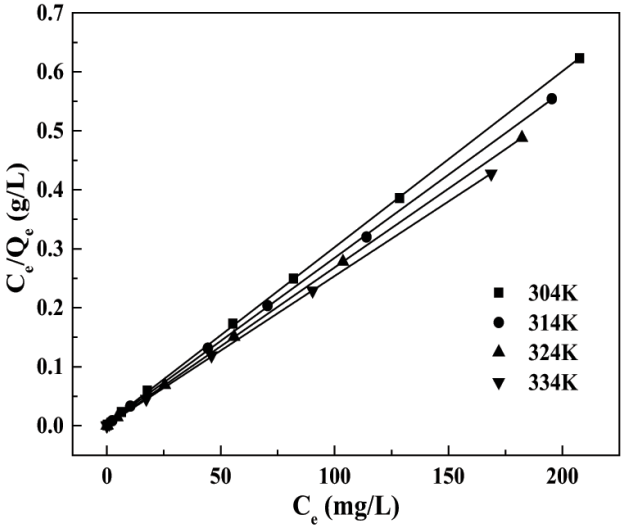

Fig. 10. Langmuir isotherm plot for adsorption of Pb^{2+} on HMO.

Table 3
Adsorption isotherm parameters of different models for Pb^{2+} adsorption on HMO

Temperature (K)	Q_{exp} (mg/g)	Langmuir			Freundlich		
		Q_{max} (mg/g)	K_L (L/mg)	R^2	n	K_F (mg/g)	R^2
304	333.0	335.6	0.6946	0.99986	12.02	225.9	0.9597
314	352.4	354.6	1.0108	0.99979	11.04	235.7	0.8898
324	373.4	374.5	2.8590	0.99998	14.05	277.2	0.8768
334	395.0	395.3	2.8224	0.99995	13.73	293.5	0.8250

Table 4
R_L values of Pb^{2+} at different initial concentrations

Temperature (K)	R_L						
c_0 (mg/L)	124	166	208	250	292	334	418
304	0.0115	0.0086	0.0069	0.0057	0.0049	0.0043	0.0034
314	0.0079	0.0059	0.0047	0.0040	0.0034	0.0030	0.0024
324	0.0028	0.0021	0.0017	0.0014	0.0012	0.0010	0.0008
334	0.0028	0.0021	0.0017	0.0014	0.0012	0.0010	0.0008

with the adsorption saturation obtained in the experiment. Therefore, Pb^{2+} adsorption of HMO followed the pseudo-second-order kinetic model better than others, that is, the adsorption reaction process belongs to chemical adsorption reaction [31].

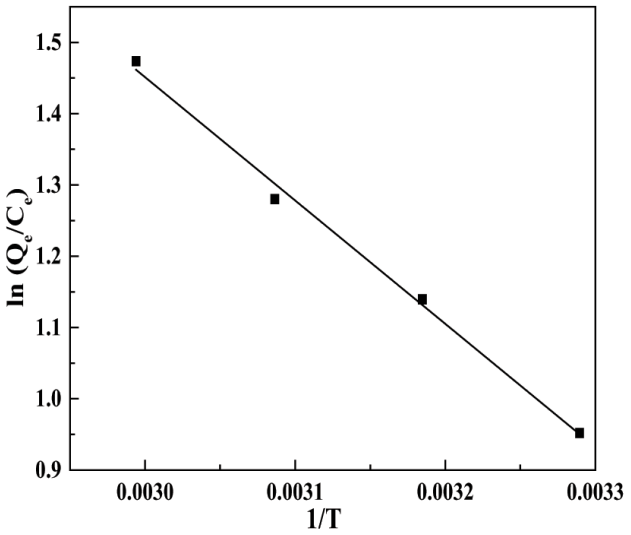

Fig. 11. Thermodynamics curve for adsorption of Pb^{2+} on HMO.

Table 5
Thermodynamic parameters for adsorption of Pb^{2+} on HMO at different temperature

T (K)	ΔG (kJ/mol)	ΔH (kJ/mol)	ΔS (J/mol K)
304	–2.40	14.39	55.22
314	–2.95		
324	–3.50		
334	–4.05		

3.4.2. Apparent activation energy of adsorption

E_a was regarded as an independent constant of temperature. Taking the data of Pb^{2+} concentration in the solution of 334 mg/L in Table 5 as an example, the values of apparent activation energy E_a and pre-exponential factor A can be obtained by linear fitting plots of ln$K$ vs. 1/T *as shown in Fig.13*. The corresponding apparent activation energy (E_a) and pre-exponential factor (A) were 7.752 kJ/mol and 0.0359, respectively.

3.5. Regeneration test

The desorption of Pb^{2+} was calculated and the effect of nitric acid concentration to Pb^{2+} in the desorption experiment was investigated. As shown in Fig. 14, the desorption rate of Pb^{2+} increased with the increase of nitric acid concentration. In this experiment, PbMO was dipped into 100 mL 2 M nitric acid to conduct the regeneration of HMO at 30°C for 120 min desorbing. After washing with deionized water until neutral, reborn HMO was used to Pb^{2+} resorption. The results are shown in Fig. 15.

As shown in Fig. 15, with the increase of regeneration times, the Pb^{2+} adsorption capacity of HMO gradually decreased. When the fourth regeneration occur, Pb^{2+} adsorption capacity of HMO decreased by 17.3%. In the process of regeneration, there will be a decrease amount in the HMO, but it had shown good regenerative adsorption performance in general. It was important to apply HMO to clean lead-containing wastewater.

3.6. Competitive adsorption

The results of single-component adsorption and mixed component adsorption are shown in Table 7. It was easy to see that, at single component adsorption, the order of the adsorption performance of HMO to toxic metal was $Pb^{2+} > Cu^{2+} > Cd^{2+} > Co^{2+} > Ni^{2+}$. As for the mixed component, the adsorption capacity of each cation of HMO all decreased, which not only further verified the order of

Table 6
Adsorption kinetic parameters of different models for Pb^{2+} adsorption on HMO

Initial concentration (mg/L)	T (K)	Pseudo-first-order			Pseudo-second-order			Intraparticle diffusion		
		Q_e (mg/g)	K_1 (1/min)	R^2	Q_e (mg/g)	K_2 (g/mg min)	R^2	K_p (mg/g min$^{0.5}$)	C (mg/g)	R^2
250	304	165.7	0.0590	0.8791	323.6	0.00155	0.9965	27.45	130.9	0.8839
	314	176.7	0.0775	0.9657	343.6	0.00169	0.9985	28.61	146.6	0.8511
	324	176.0	0.0709	0.9584	373.1	0.00169	0.9983	28.49	175.3	0.8830
	334	171.1	0.0792	0.9602	386.1	0.00196	0.9990	28.00	195.1	0.8356
334	304	167.5	0.0631	0.9540	1.629	0.00160	0.9970	26.92	147.6	0.8936
	314	159.0	0.0708	0.9060	1.740	0.00197	0.9988	26.76	177.4	0.8481
	324	144.7	0.0564	0.8868	1.808	0.00201	0.9976	23.93	206.9	0.8672
	334	163.6	0.0787	0.9244	1.924	0.00215	0.9993	27.72	211.9	0.8151
418	304	164.7	0.0870	0.9563	1.635	0.00205	0.9994	27.36	154.4	0.8113
	314	171.7	0.0703	0.9598	1.726	0.00170	0.9982	27.69	164.7	0.8878
	324	167.3	0.0835	0.9848	1.828	0.00203	0.9989	26.34	197.9	0.8746
	334	160.6	0.1145	0.9871	1.931	0.00282	0.9997	25.14	234.2	0.7879

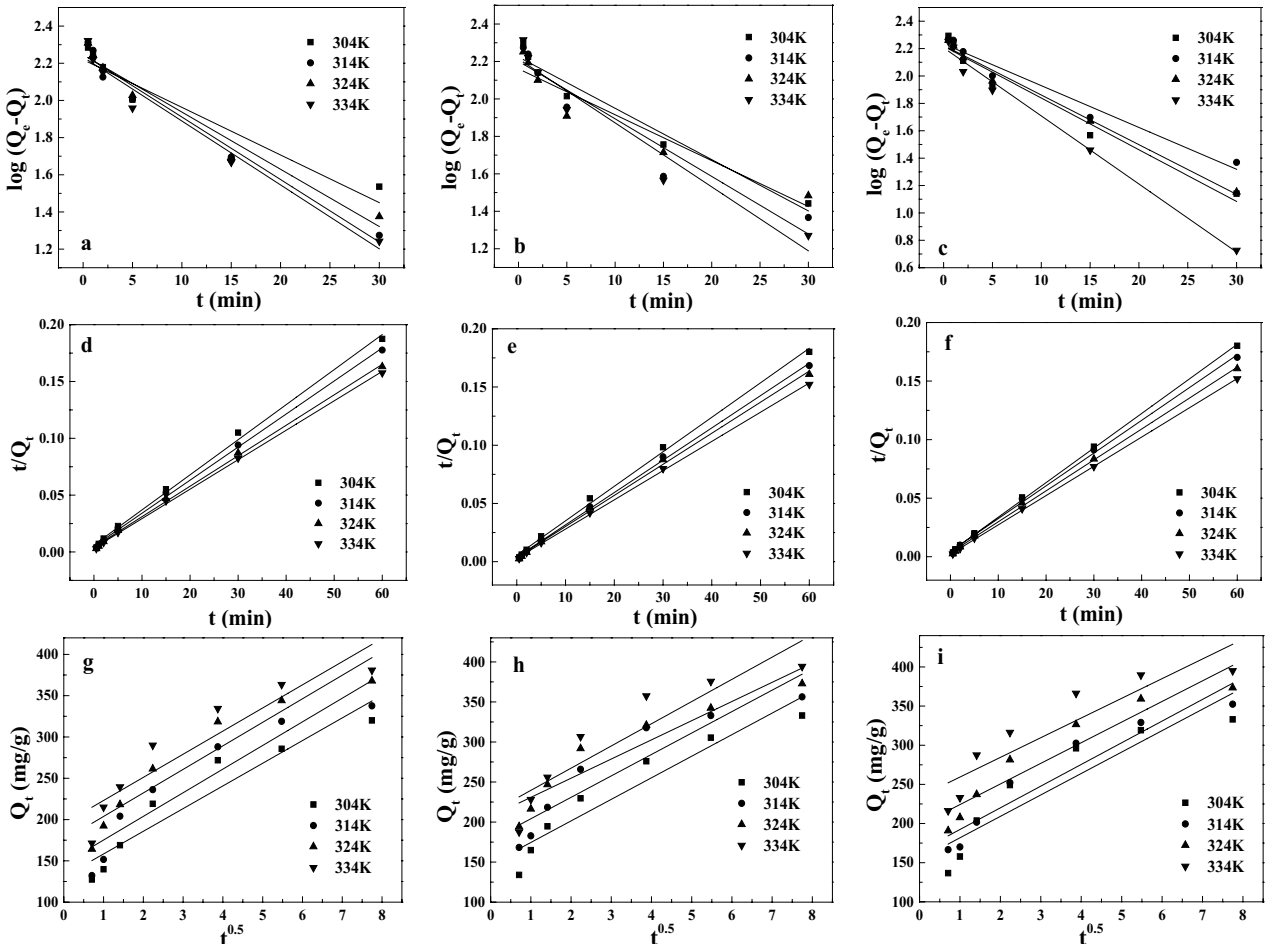

Fig. 12. Linear plot of adsorption kinetic model for adsorption of Pb^{2+} on HMO: (a–c) pseudo-first-order model for 250, 334, and 418 mg/L, respectively; (d–f) pseudo-second-order model for 250, 334, and 418 mg/L, respectively; (g–i) intraparticle diffusion kinetic model for 250, 334, and 418 mg/L, respectively).

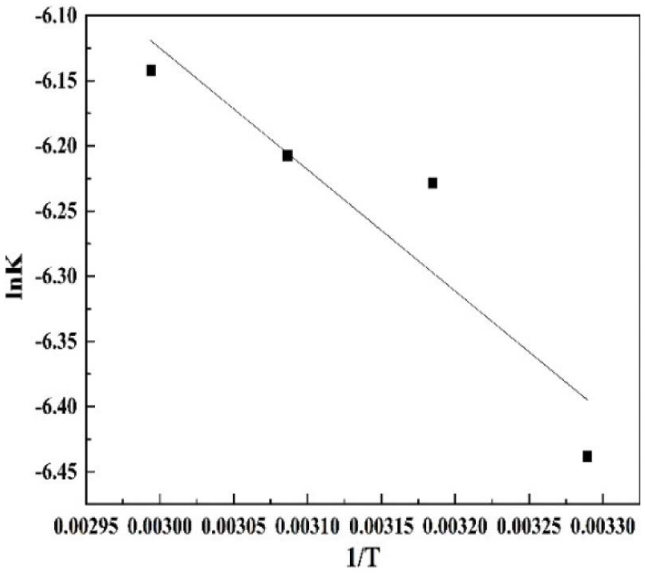

Fig. 13. Linear plot of Arrhenius empirical expression.

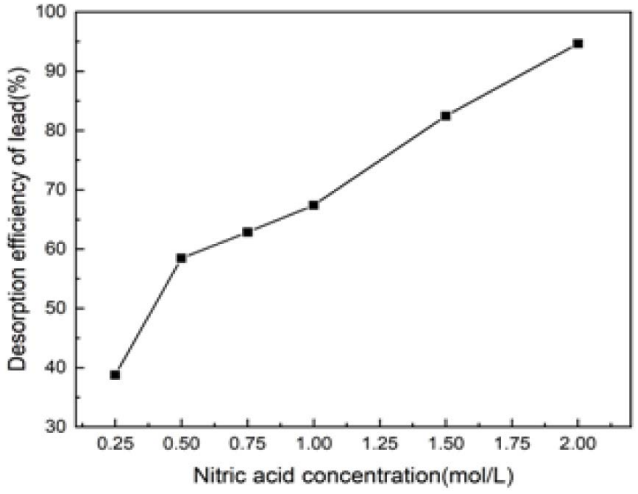

Fig. 14. Effect of HNO_3 concentration on the regeneration performance of HMO.

adsorption performance of metals of HMO, but also indicated that HMO had strong adsorption selectivity for them.

3.7. Characterization of adsorbents in the preparation process

3.7.1. Phase analysis

To explore the reaction mechanism of NaOH and pyrolusite in the roasting process and the phase transformation in the water washing and pickling process, the roasting product, washing product, and pickling product (the adsorbent of this study) were prepared under the most optimal conditions (roasting temperature was 400°C, the alkali–solid ratio was 1:1, roasting time was 120 min, and HCl concentration was 1 mol/L) and samples in this study were characterized by XRD.

The XRD patterns of the various stages in the roasting–washing process are shown in Fig. 16. Major phases in the roasting product were Na_2SiO_3, $Na_{0.5}FeO_2$, $Na_{17}Al_5O_{16}$, and SiO_2. The results indicated that the diffraction peaks of Na_2SiO_3 and $Na_{17}Al_5O_{16}$ in the water-washing solid were almost absent, which illustrated that Na_2SiO_3 and $Na_{17}Al_5O_{16}$ were removed by water washing. $Na_{0.5}FeO_2$ dissolved in an acid solution and was removed by pickling because the diffraction peak of $Na_{0.5}FeO_2$ in the adsorbent failed to detect. The diffraction peak of $Na_{0.55}Mn_2O_4{\cdot}1.5H_2O$ appeared in water-washed solid and adsorbent, but didn't detect in the roasting product. The content of impurities (Na_2SiO_3, $Na_{0.5}FeO_2$, and $Na_{17}Al_5O_{16}$) in the roasting product were extremely high, which caused $Na_{0.55}Mn_2O_4{\cdot}1.5H_2O$ in the roasting product to be wrapped and present a poor crystalline phase. According to the XRD, XRF, and XPS results of pyrolusite, it was known that the main composition of pyrolusite were SiO_2, HMOs, iron oxides, and aluminum oxides. Thus, it can be inferred that HMOs, silicon dioxide, iron oxides, and aluminum oxides in the pyrolusite reacted with NaOH to form $Na_{0.55}Mn_2O_4{\cdot}1.5H_2O$, Na_2SiO_3, $Na_{0.5}FeO_2$, and $Na_{17}Al_5O_{16}$ in the anaerobic alkali roasting process, respectively. Then in the acid pickling process, $Na_{0.55}Mn_2O_4{\cdot}1.5H_2O$ would translate into $H_{0.55}Mn_2O_4{\cdot}1.5H_2O$ due to the exchange of hydrogen ions and sodium ions. The main reaction equations in the roasting–washing process were as follows:

$$Mn_xO_y + NaOH \rightarrow Na_{0.55}Mn_2O_4 \cdot 1.5H_2O \quad (24)$$

$$SiO_2 + 2NaOH \rightarrow Na_2SiO_3 + H_2O \quad (25)$$

$$Fe_xO_y + NaOH \rightarrow Na_{0.5}FeO_2 + H_2O \quad (26)$$

$$Al_xO_y + NaOH \rightarrow Na_{17}Al_5O_{16} + H_2O \quad (27)$$

$$Na_{0.5}Mn_2O_4 \cdot 1.5H_2O \xrightarrow{\text{Pickling}} H_{0.55}Mn_2O_4 \cdot 1.5H_2O \quad (28)$$

3.7.2. Elemental analysis

Compared with the chemical composition of pyrolusite, Table 1 also shows that Mn content increased from 28.54% to 48.03%, and Si content decreased from 19.07% to 1.62% and other impurities content was all reduced through

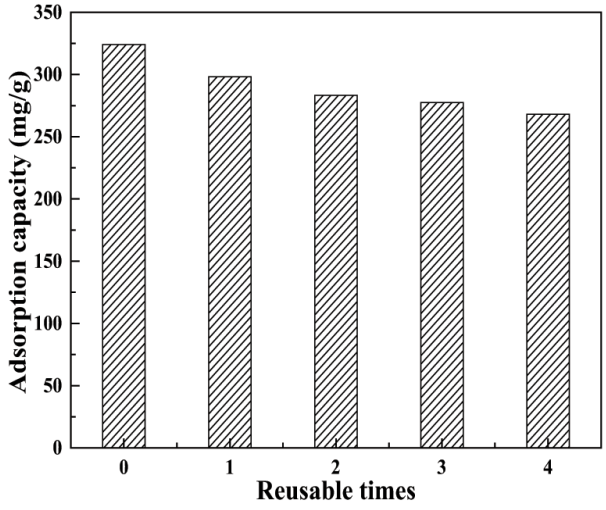

Fig. 15. Effect of reusable times on the regeneration performance of HMO.

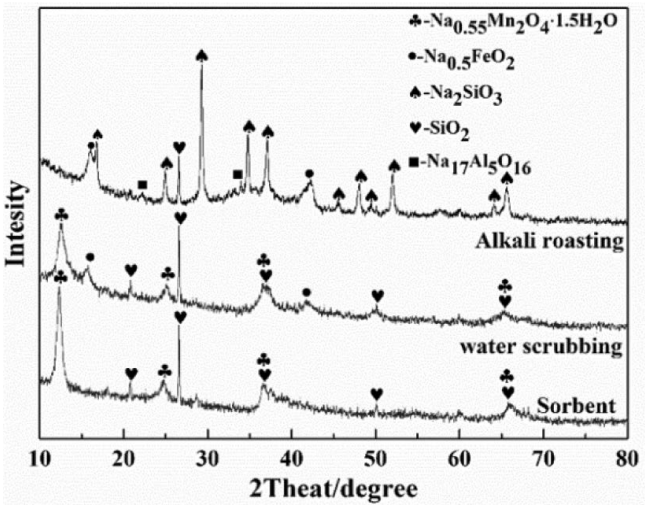

Fig. 16. X-ray diffraction pattern of HMO preparing process.

Table 7
Adsorption capacity of HMO (mg/g)

	$Q_{(Pb)}$	$Q_{(Cu)}$	$Q_{(Cd)}$	$Q_{(Co)}$	$Q_{(Ni)}$
Single component adsorption	327.2	57.44	66.88	27.84	10.72
Mixed component adsorption	283	14.72	3.2	1.76	0

roasting–washing treatment. Although the mass percentage of iron, nickel, and titanium were slightly increased, they were partially removed due to the large reduction in the total mass of solids. Therefore, the HMO was prepared from low-grade pyrolusite by anaerobic alkali roasting–washing method, which removed most impurities in pyrolusite and improved the Mn content and the adsorption performance on toxic metal.

3.7.3. SEM analysis

To observe clearly the surface topography of pyrolusite and HMO, the SEM micrograph of pyrolusite (a) and HMO (b) obtained are shown in Fig. 17. Fig. 17a shows that the surface of MO was rich in strips and block material arranged irregularly and had few voids, which formed agglomeration. While Fig. 17b indicates that the number of voids on the surface of HMO increased and the particle size became small. Such change was more conducive to the flow of the adsorbate inside the HMO, in other words, it facilitated the internal diffusion of toxic metal ions in the adsorption process, which fully improved the adsorption capacity of HMO on toxic metals ions.

3.7.4. BET analysis

Table 8 shows the specific surface area and pore size parameters of pyrolusite and HMO. It can be seen from Table 8 that the specific surface area of manganese ore increased from 31.21 to 57.41 m^2/g after NaOH roasting without oxygen. The total pore volume also increased from 0.11 to 0.14 cm^3/g, which contained a large number of mesoporous holes and a small number of micropores. Figs. 18 and 19 show that N_2 adsorption–desorption isotherms of pyrolusite and HMO belong to the fourth type of curve in BDDT, and small hysteresis rings appearing belong to the H_3 type, which indicates that these two materials are mesoporous materials [47,48].

3.7.5. Infrared analysis

The infrared analysis of pyrolusite and HMO was carried out respectively, and its infrared spectrum is shown in Fig. 20.

For the adsorbent, there were four absorption peaks in its infrared spectrum, the corresponding peaks at 1,628 and 3,379 cm^{-1} were the bending and stretching vibration absorption peaks of the surface hydroxyl group, the absorption peaks at 513 and 470 cm^{-1} were caused by Mn–O vibration and the absorption peaks at 1,082 cm^{-1} were Si–O absorption peaks.

Both pyrogen and sorbent had hydroxyl, Mn–O, and Si–O absorption peaks. Compared with pyrogen, there were fewer miscellaneous peaks of sorbent, and the Si–O absorption peak intensity detected by sorbent was far less than pyrogen. At the same time, Fe–O characteristic peak

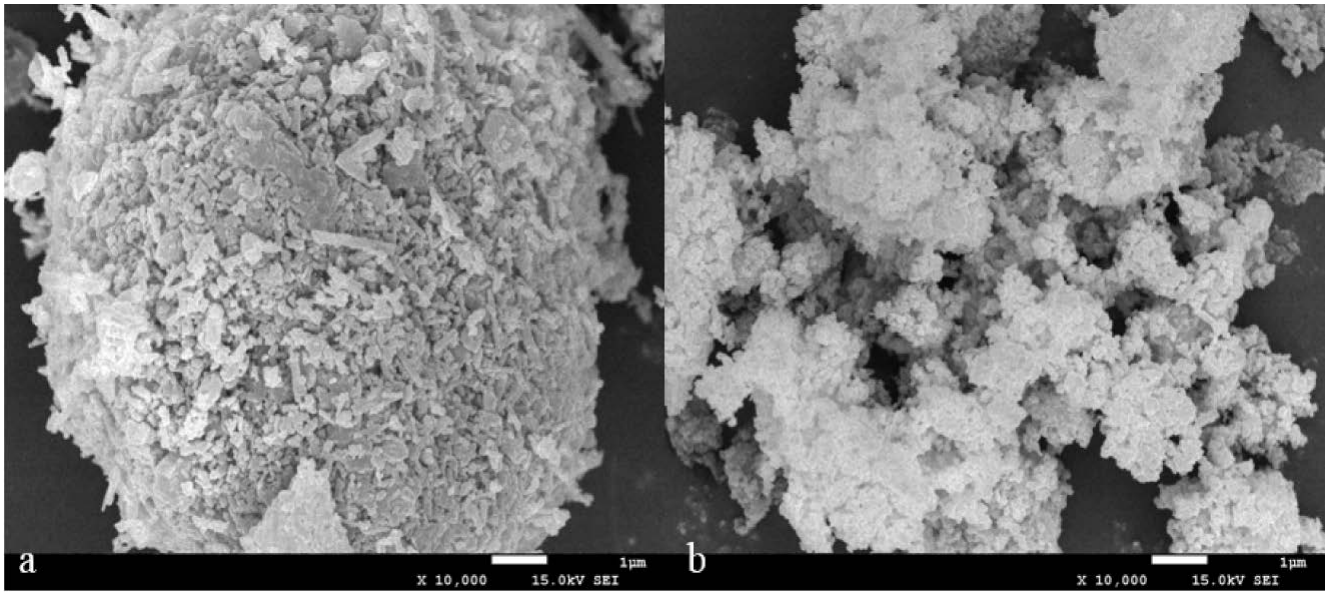

Fig. 17. SEM pattern of pyrolusite and adsorbent.

Table 8
Specific surface area and pore size parameters of pyrolusite and HMO

Sample	Surface area (m^2/g)	Micropore volume (cm^3/g)	Mesopore volume (cm^3/g)	Total pore volume (cm^3/g)	Average pore diameter (nm)
Adsorbent	57.41	0.01	0.12	0.14	9.40
Pyrolusite	31.21	0.01	0.10	0.11	14.60

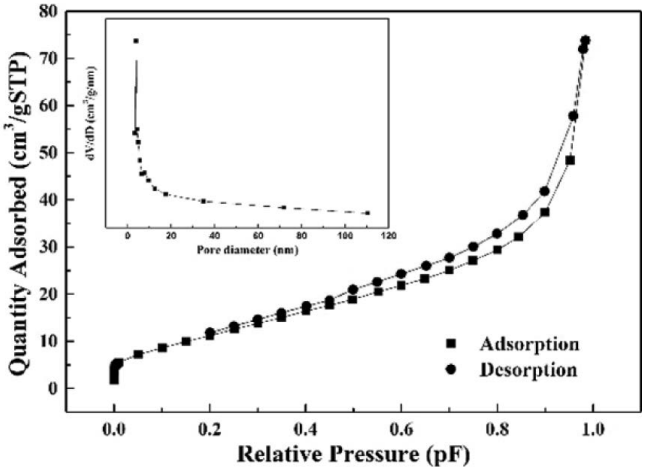

Fig. 18. N_2 adsorption–desorption isotherms for sample pyrolusite.

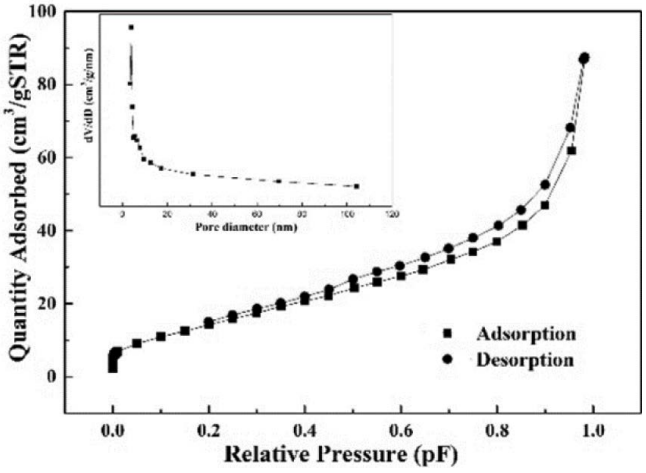

Fig. 19. N_2 adsorption–desorption isotherms for sample adsorbent.

appeared in the infrared spectrum of pyrolusite, while adsorbent did not have Fe–O characteristic peak, which indicated that most of the silicon dioxide, iron oxide, and other impurities in pyrolusite were removed through the process of roasting, washing, and acid washing without oxygen.

3.8. Characterization of absorbents in the adsorption process

3.8.1. XRD analysis

The XRD analyzer was used to analyze the material changes before (HMO) and after the adsorption of Pb^{2+} (PbMO). XRD pattern (Fig. 21) show that the $Na_{0.55}Mn_2O_4{\cdot}1.5H_2O$ diffraction peak appeared in 2θ = 12.23° and 24.63° and 36.67° and 66.1° before adsorption, however, the $Na_{0.55}Mn_2O_4{\cdot}1.5H_2O$ diffraction peak didn't appear in the XRD spectrum of PbMO. At the same time, the $Pb_{2-x}Mn_8O_{16}$ ($0 < x < 2$) diffraction peak appeared near the disappearing diffraction peak, showing that HMO of $Na_{0.55}Mn_2O_4{\cdot}1.5H_2O$ reacted with Pb^{2+} in the solution and $Pb_{2-x}Mn_8O_{16}$ was formed. The adsorbent had a chemical adsorption effect on Pb^{2+}.

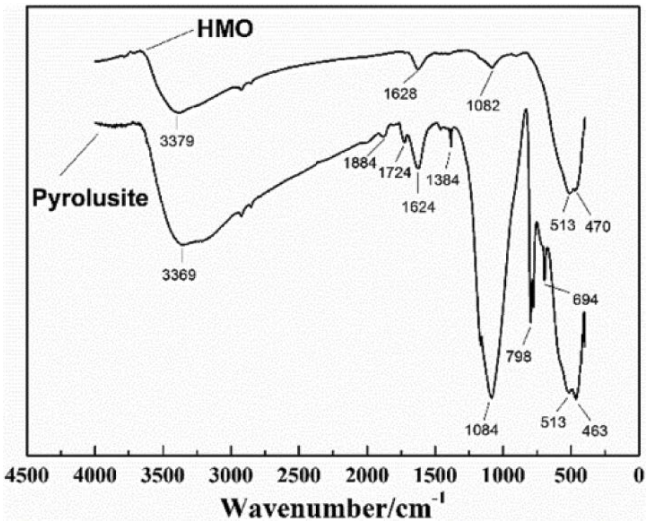

Fig. 20. Infrared spectra analysis of pyrolusite and adsorbent.

3.8.2. EDS analysis

X-ray energy spectrum analysis (EDS) was used to analyze the changes of the chemical composition of HMO and PbMO. The spectrum is shown in Fig. 22.

It can be seen from the figure that the surface of PbMO distributed lots of white materials, meaning that Pb^{2+} was actually adsorbed in HMO.

3.8.3. Infrared analysis

The infrared characterization of HMO and PbMO is analyzed in Fig. 23.

As for HMO, bands at 1,628 and 3,379 cm^{-1} were telescopic vibration and flexural vibration absorption peaks of surface hydroxyl groups, respectively. Big and wide peaks said large amounts of hydroxyl on the surface of HMO, and after the adsorption of lead ions, these peaks shifted to 1,624 and 3,367 cm^{-1} showing that hydroxyl groups complexed with lead ions to form Pb–O bonds [49]. In addition, peaks at 513 and 470 cm^{-1} are typical Mn–O peaks [50] which shifted to 517 cm^{-1} after Pb^{2+} adsorption and whose intensity increased indicating that more Mn–O bonds were formed after Pb^{2+} adsorption. It can be inferred that Mn–O–H combined with lead ions to form Mn–O–Pb bonds. The peak of Si–O was at 1,082 cm^{-1} [51], and there was no change in HMO and PbMO, suggesting that HMO also contained SiO_2, which was consistent with the results of XRD analysis. Comparing the two infrared spectra, it was found that a new absorption peak belonging to nitrate ions appeared in the infrared spectra of Pb–MO, whose wave number was 1.384 cm^{-1}.

3.8.4. XPS analysis

Samples of HMO and PbMO were respectively analyzed by XPS scanning, and their spectra are shown in Fig. 24a. The full spectrum of XPS depicted that characteristic optoelectronic lines of Mn2p and O1s appeared in the samples of HMO and PbMO, and characteristic optoelectronic

lines of Pb4f appeared in the samples of PbMO at the same time.

In order to further investigate the changes of chemical states of each element of HMO during Pb^{2+} adsorption, the narrow spectra of Mn2p, O1s, and Pb4f were scanned, and results are shown in Figs. 24b–d. As it can be seen from Fig. 24b, there were four peaks on HMO and PbMO, which were peaks of $Mn2p_{3/2}$ and $Mn2p_{1/2}$, respectively. The binding energies of Mn2p of HMO were 641.9, 642.6, 653.1, and 654.3 eV [51,52], respectively, while the binding energies of Mn2p of PbMO were 641.7, 642.7, 653.0, and 653.8 eV, respectively. However, the binding energies of Mn2p of MnO, MnOOH, MnO_2 were 640.2, 641.5, and 642.2, respectively, which indicated that HMO and PbMO mainly contained Mn(III) and Mn(IV), and the content of Mn(IV) was more than Mn(III). The binding energies of O1s of HMO were

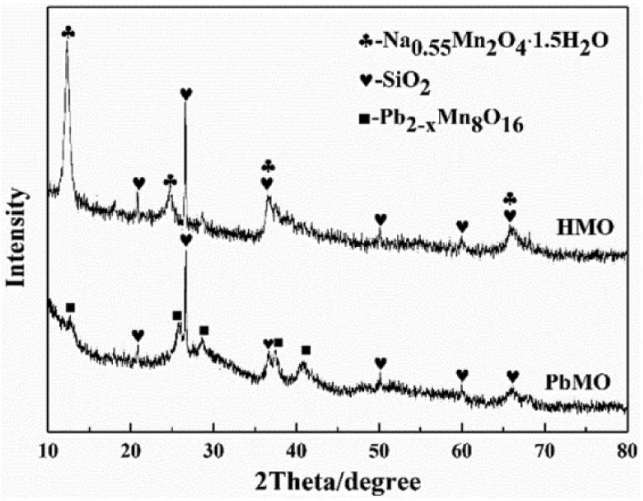

Fig. 21. X-ray diffraction pattern of HMO and PbMO.

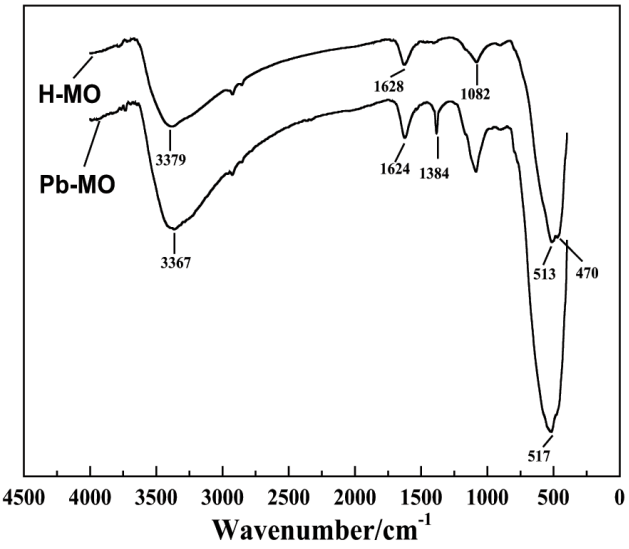

Fig. 23. Infrared spectra analysis of HMO and PbMO.

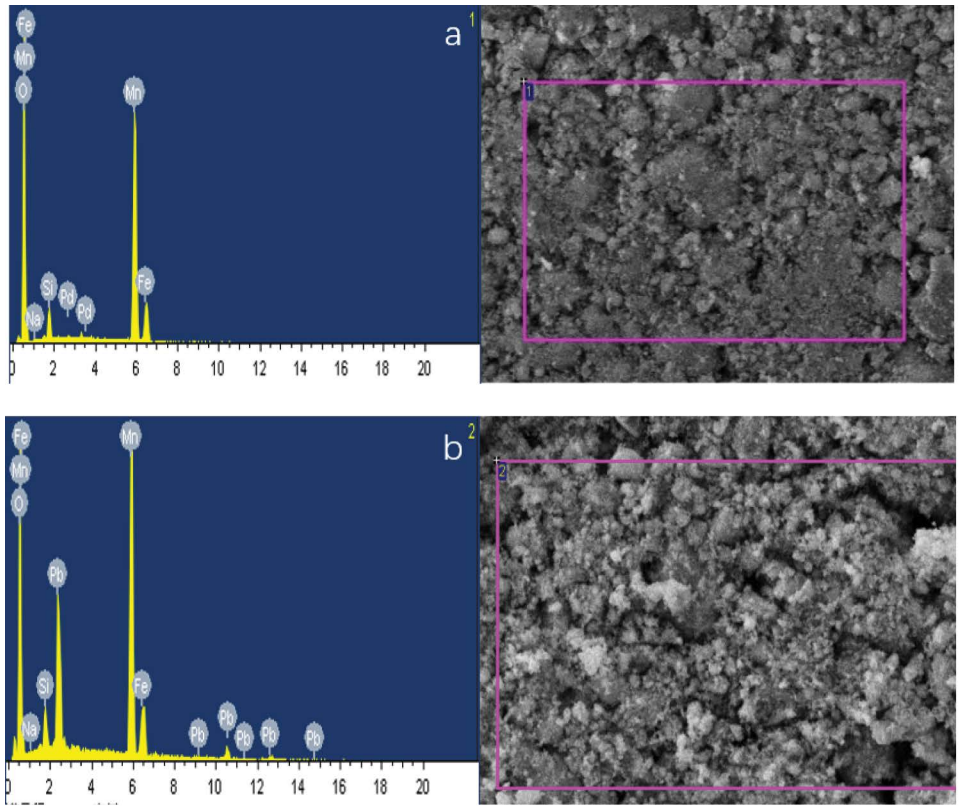

Fig. 22. EDS pattern for before and after adsorption of Pb^{2+} on HMO: (a) HMO and (b) PbMO.

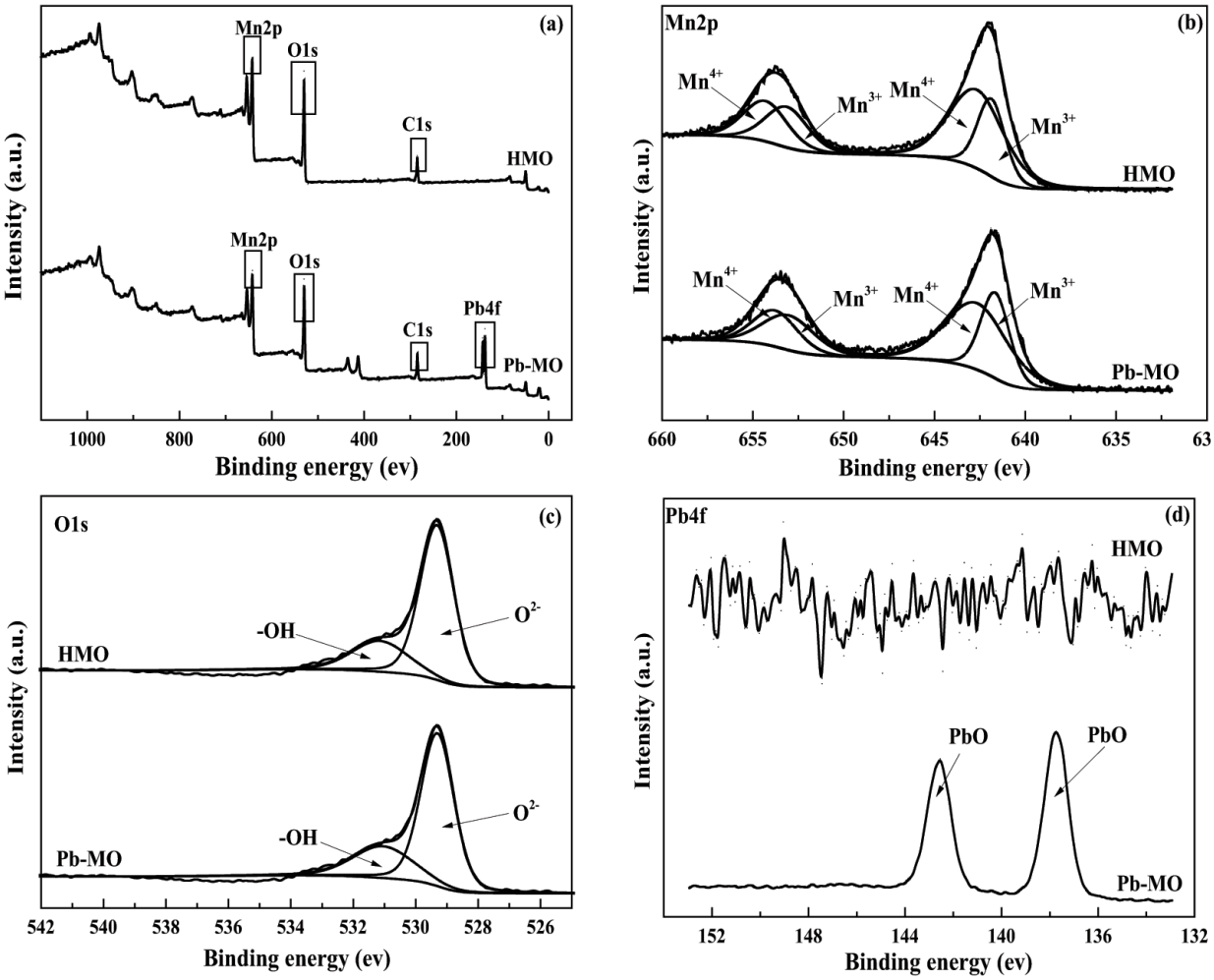

Fig. 24. XPS full spectra (a), Mn2p (b), O1s (c), and Pb4f (d) peak spectra of HMO and PbMO.

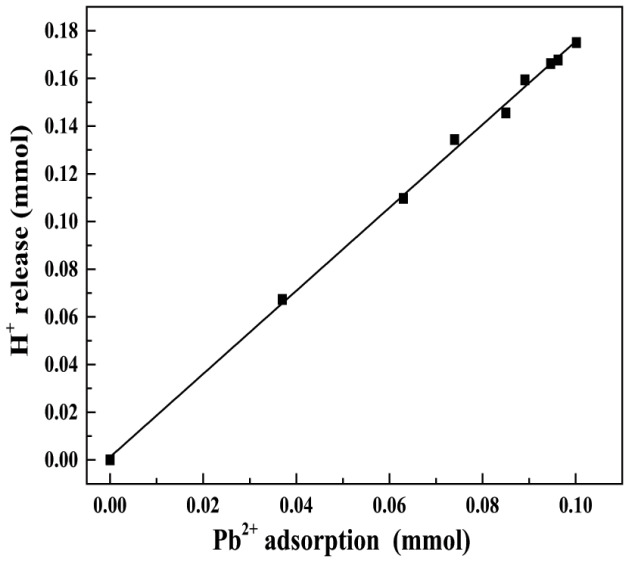

Fig. 25. Linear plot of H^+ release and Pb^{2+} adsorption amount.

529.3 and 531.1 eV, respectively, while the binding energies of O1s of PbMO were 529.5 and 531.4 eV, respectively. In addition, peaks around 529.5 and 531.4 eV belonged to the oxygen (metal-bonded oxygen) in the lattice and the oxygen (–OH) in the surface hydroxyl group [53]. By comparing the peak area of oxygen in lattice oxygen and hydroxyl of HMO and PbMO, results showed that the ratio of peak area increased from 32.9% to 37.7%. The possible reason was that Pb^{2+} may be hydrolyzed into $PbOH^+$ in an aqueous solution and adsorbed by HMO leading to increase of oxygen in the surface hydroxyl group [11,54]. Characteristic photoelectron lines of Pb4f of HMO were failed to detect, while peaks of $Pb4f_{5/2}$ and $Pb4f_{7/2}$ of PbMO were detected, which belong to characteristic peak of Pb–O. The binding energies were 143.1 and 138.2 eV, respectively [54], illustrating that Pb^{2+} complexed with the hydroxyl group on the surface of HMO.

3.8.5. Relationship between the adsorption amount of Pb^{2+} and the release amount of H^+ during adsorption progress by HMO

This experiment investigated the relationship between the adsorption amount of Pb^{2+} and the release amount of

H^+ at different initial concentrations, as shown in Fig. 25. There was a good linear determination between H^+ release amount and Pb^{2+} adsorption amount in the adsorption process, and the fitting relation was $y = 1.743x + 0.00123$, $R^2 = 0.9979$. This indicated that the lead element was mainly adsorbed in Pb^{2+} and $PbOH^+$ forms by HMO the molar ratio of Pb^{2+} and $PbOH^+$ adsorbed was 0.743:0.257, which was consistent with the result of XPS. We can get the conclusion that complexation prevailed in this adsorption process.

4. Conclusion

In this paper, a low-cost and efficient HMO adsorbent (HMO) for Pb^{2+} removal was prepared with good channel structure, higher Mn content, and larger adsorption capacity using low-grade pyrolusite by the pyrolusite–NaOH molten roasting and washing processes. The influencing factors experiments showed that the optimal dosage and equilibrium adsorption time of HMO in the process of lead ion adsorption were 0.625 g/L and 60 min, respectively. The increase of pH, initial concentration, and temperature were all favorable for adsorption progress. However, Pb^{2+} would hydrolyze with higher pH value, and value of pH was controlled at 5.0. In addition, the adsorbed equilibrium amount of 395.0 mg/g was obtained under the optimized conditions.

In pyrolusite–NaOH molten roasting process under the oxygen-deprived conditions, Si, Mn, Fe, and Al were calcinated with NaOH in the absence of oxygen to generate Na_2SiO_3, $Na_{0.55}Mn_2O_4{\cdot}1.5H_2O$, $Na_{0.5}FeO_2$, $Na_{17}Al_5O_{16}$, and other products, among which Na_2SiO_3 and $Na_{17}Al_5O_{16}$ were removed by water washing, and $Na_{0.5}FeO_2$ was removed by acid washing, and $Na_{0.55}Mn_2O_4{\cdot}1.5H_2O$ was transformed into $H_{0.55}Mn_2O_4{\cdot}1.5H_2O$. Pb^{2+} had been adsorbed on HMO during the adsorption process, because of the generating of $Pb_{2-x}Mn_8O_{16}$ substances on HMO surface.

The adsorption process was monolayer adsorption, and the results of adsorption thermodynamics showed that the adsorption process was a spontaneous and endothermic reaction. The results of adsorption kinetics demonstrated that the adsorption process agreed with pseudo-secondary kinetics, and the corresponding apparent activation energy (E_a) and preexponential factor (A) were 7.752 kJ/mol and 0.0359, respectively.

The effect of each metal of HMO was different and the order was $Pb^{2+} > Cu^{2+} > Cd^{2+} > Co^{2+} > Ni^{2+}$. HMO showed great adsorption ability and regeneration performance in removal.

The results of XRD and EDS showed that lead ions in the solution had been adsorbed on the surface of HMO and $Pb_{2-x}Mn_8O_{16}$ appeared. In addition, IR and XPS showed that Pb^{2+} adsorption on HMO mainly depended on complexation reaction among hydroxyl groups on the surface and lead ions in the solution. Finally, the fitting results of H^+ release amount and Pb^{2+} adsorption amount in the adsorption process further confirmed that lead element was adsorbed on the adsorbent surface only in the form of Pb^{2+} and $PbOH^+$, and the molar ratio of Pb^{2+} and $PbOH^+$ was 0.743:0.257.

Acknowledgments

This project is supported by the National Natural Science Foundation of China (NSFC-51304140 and NSFC-51374150).

References

[1] S.T. El-Wakeel, R.S. El-Tawil, H.A.M. Abuzeid, A.E. Abdel-Ghany, A.M. Hashem, Synthesis and structural properties of MnO_2 as adsorbent for the removal of lead (Pb^{2+}) from aqueous solution, J. Taiwan Inst. Chem. Eng., 72 (2017) 95–103.
[2] L. Bulgariu, D. Bulgariu, Functionalized soy waste biomass - a novel environmental-friendly biosorbent for the removal of heavy metals from aqueous solution, J. Cleaner Prod., 197 (2018) 875–885.
[3] T.A. Kurniawan, G.Y.S. Chan, W.H. Lo, S. Babel, Physico-chemical treatment techniques for wastewater laden with heavy metals, Chem. Eng. J., 118 (2006) 83–98.
[4] X.H. Feng, L.M. Zhai, W.F. Tan, F. Liu, J.Z. He, Adsorption and redox reactions of heavy metals on synthesized Mn oxide minerals, Environ. Pollut., 147 (2007) 366–373.
[5] D. Afzali, M. Fayazi, Deposition of MnO_2 nanoparticles on the magnetic halloysite nanotubes by hydrothermal method for lead(II) removal from aqueous solutions, J. Taiwan Inst. Chem. Eng., 63 (2016) 421–429.
[6] M. Fayazi, D. Afzali, R. Ghanei-Motlagh, A. Iraji, Synthesis of novel sepiolite-iron oxide-manganese dioxide nanocomposite and application for lead(II) removal from aqueous solutions, Environ. Sci. Pollut. Res., 26 (2019) 18893–18903.
[7] B.A.M. Al-Rashdi, D.J. Johnson, N. Hilal, Removal of heavy metal ions by nanofiltration, Desalination, 315 (2013) 2–17.
[8] V.O. Kaptakov, V.V. Milyutin, N.A. Nekrasova, Behavior of alkali metal and ammonium salts in nanofiltration of their aqueous solutions, Radiochemistry, 61 (2019) 203–206.
[9] P.R. Choudhury, S. Majumdar, G.C. Sahoo, S. Saha, P. Mondal, High pressure ultrafiltration CuO/hydroxyethyl cellulose composite ceramic membrane for separation of Cr(VI) and Pb(II) from contaminated water, Chem. Eng. J., 336 (2018) 570–578.
[10] K. Sunil, G. Karunakaran, S. Yadav, M. Padaki, V. Zadorozhnyy, R.K. Pai, Al-Ti_2O_6 a mixed metal oxide based composite membrane: a unique membrane for removal of heavy metals, Chem. Eng. J., 348 (2018) 678–684.
[11] M. Xu, H.J. Wang, D. Lei, D. Qu, Y.J. Zhai, Y.L. Wang, Removal of Pb(II) from aqueous solution by hydrous manganese dioxide: adsorption behavior and mechanism, J. Environ. Sci., 25 (2013) 479–486.
[12] Q.D. Qin, Q.Q. Wang, D.F. Fu, J. Ma, An efficient approach for Pb(II) and Cd(II) removal using manganese dioxide formed *in situ*, Chem. Eng. J., 172 (2011) 68–74.
[13] Y.L. Ma, L. Lv, Y.R. Guo, Y.J. Fu, Q. Shao, T.T. Wu, S.J. Guo, K. Sun, X.K. Guo, E.K. Wujcik, Z.H. Guo, Porous lignin based poly (acrylic acid)/organo-montmorillonite nanocomposites: swelling behaviors and rapid removal of Pb(II) ions, Polymer, 128 (2017) 12–23.
[14] Q.T. Shi, A. Terracciano, Y. Zhao, C.Y. Wei, C. Christodoulatos, X.G. Meng, Evaluation of metal oxides and activated carbon for lead removal: kinetics, isotherms, column tests, and the role of co-existing ions, Sci. Total Environ., 648 (2019) 176–183.
[15] L.Y. Wang, L.Q. Yang, Y.F. Li, Y. Zhang, X.J. Ma, Z.F. Ye, Study on adsorption mechanism of Pb(II) and Cu(II) in aqueous solution using PS-EDTA resin, Chem. Eng. J., 163 (2010) 364–372.
[16] A. Afkhami, M. Saber-Tehrani, H. Bagheri, Simultaneous removal of heavy-metal ions in wastewater samples using nano-alumina modified with 2,4-dinitrophenylhydrazine, J. Hazard. Mater., 181 (2010) 836–844.
[17] M.A. Tofighy, T. Mohammadi, Adsorption of divalent heavy metal ions from water using carbon nanotube sheets, J. Hazard. Mater., 185 (2011) 140–147.
[18] E.J. Kim, C.S. Lee, Y.Y. Chang, Y.S. Chang, Hierarchically structured manganese oxide-coated magnetic nanocomposites for the efficient removal of heavy metal ions from aqueous systems, ACS Appl. Mater. Interfaces, 5 (2013) 9628–9634.
[19] N.C. Le, D. Van Phuc, Sorption of lead(II), cobalt(II) and copper(II) ions from aqueous solutions by γ-MnO_2 nanostructure, Adv. Nat. Sci.: Nanosci. Nanotechnol., 6 (2015) 025014, doi: 10.1088/2043-6262/6/2/025014.
[20] H.P. Zhang, A.B. Wu, H.Y. Fu, L. Zhang, H. Liu, S.R. Zheng, H.Q. Wan, Z.Y. Xu, Efficient removal of Pb(II) ions using

manganese oxides: the role of crystal structure, RSC Adv., 7 (2017) 41228–41240.
[21] Q. Su, B.C. Pan, S.L. Wan, W.M. Zhang, L. Lv, Use of hydrous manganese dioxide as a potential sorbent for selective removal of lead, cadmium, and zinc ions from water, J. Colloid Interface Sci., 349 (2010) 607–612.
[22] G.K. Sarma, S. Sen Gupta, K.G. Bhattacharyya, Nanomaterials as versatile adsorbents for heavy metal ions in water: a review, Environ. Sci. Pollut. Res., 26 (2019) 6245–6278.
[23] Q.Q. Yu, T. Ohnuki, N. Kozai, F. Sakamoto, K. Tanaka, K. Sasaki, Quantitative analysis of radiocesium retention onto birnessite and todorokite, Chem. Geol., 470 (2017) 141–151.
[24] J.L. Wang, J.E. Li, C.J. Jiang, P. Zhou, P.Y. Zhang, J.G. Yu, The effect of manganese vacancy in birnessite-type MnO_2 on room-temperature oxidation of formaldehyde in air, Appl. Catal., B, 204 (2017) 147–155.
[25] S. Ziller, J.F. von Bulow, S. Dahl, M. Linden, A fast sol–gel synthesis leading to highly crystalline birnessites under non-hydrothermal conditions, Dalton Trans., 46 (2017) 4582–4588.
[26] C.X. He, F.C. Xie, Adsorption behavior of manganese dioxide towards heavy metal ions: surface zeta potential effect, Water Air Soil Pollut., 229 (2018) 77, doi: 10.1007/s11270-018-3712-6.
[27] Y. Wang, X.H. Feng, M. Villalobos, W.F. Tan, F. Liu, Sorption behavior of heavy metals on birnessite: relationship with its Mn average oxidation state and implications for types of sorption sites, Chem. Geol., 292 (2012) 25–34.
[28] I.A. Oke, N.O. Olarinoye, S.R.A. Adewusi, Adsorption kinetics for arsenic removal from aqueous solutions by untreated powdered eggshell, Adsorption, 14 (2008) 73–83.
[29] C.S. Jeon, K. Baek, J.K. Park, Y.K. Oh, S.D. Lee, Adsorption characteristics of As(V) on iron-coated zeolite, J. Hazard. Mater., 163 (2009) 804–808.
[30] S. Kocaoba, Y. Orhan, T. Akyüz, Kinetics and equilibrium studies of heavy metal ions removalby use of natural zeolite, Desalination, 214 (2007) 1–10.
[31] J. Febrianto, A.N. Kosasih, J. Sunarso, Y.H. Ju, N. Indraswati, S. Ismadji, Equilibrium and kinetic studies in adsorption of heavy metals using biosorbent: a summary of recent studies, J. Hazard. Mater., 162 (2009) 616–645.
[32] T.A. Khan, S.A. Chaudhry, I. Ali, Thermodynamic and kinetic studies of As(V) removal from water by zirconium oxide-coated marine sand, Environ. Sci. Pollut. Res., 20 (2013) 5425–5440.
[33] I.H. Lee, Y.C. Kuan, J.M. Chern, Equilibrium and kinetics of heavy metal ion exchange, J. Chin. Inst. Chem. Eng., 38 (2007) 71–84.
[34] A. Sari, M. Tuzen, Cd(II) adsorption from aqueous solution by raw and modified kaolinite, Appl. Clay Sci., 88–89 (2014) 63–72.
[35] Y. Cantu, A. Remes, A. Reyna, D. Martinez, J. Villarreal, H. Ramos, S. Trevino, C. Tamez, A. Martinez, T. Eubanks, J.G. Parsons, Thermodynamics, kinetics, and activation energy studies of the sorption of chromium(III) and chromium(VI) to a Mn_3O_4 nanomaterial, Chem. Eng. J., 254 (2014) 374–383.
[36] X.Y. Deng, Y.L. Feng, H.R. Li, Z.W. Du, J.X. Kang, C.L. Guo, Preparation of sodium manganate from low-grade pyrolusite by alkaline predesilication-fluidized roasting technique, Trans. Nonferrous Met. Soc. China, 28 (2018) 1045–1052.
[37] N.A.M. Deraz, Physicochemical properties and catalytic behavior of magnesia supported manganese oxide catalysts, Thermochim. Acta, 421 (2004) 171–177.
[38] A. Zhang, Z. Zhang, J. Chen, W. Sheng, L. Sun, J. Xiang, Effect of calcination temperature on the activity and structure of MnO/TiO_2 adsorbent for Hg0 removal, Fuel Process. Technol., 135 (2015) 25–33.
[39] M.Z. Wu, W.C. Zhan, Y. Guo, Y.S. Wang, Y.L. Guo, X.Q. Gong, L. Wang, G.Z. Lu, Solvent-free selective oxidation of cyclohexane with molecular oxygen over manganese oxides: effect of the calcination temperature, Chin. J. Catal., 37 (2016) 184–192.
[40] J.S. Zhou, X.X. Zhou, K.L. Yang, Z. Gao, Z.N. Wang, C.C. Zhou, S.A. Baig, X.H. Xu, Adsorption behavior and mechanism of arsenic on mesoporous silica modified by iron-manganese binary oxide ($FeMnO_3$/SBA-15) from aqueous systems, J. Hazard. Mater., 384 (2020) 121229, doi: 10.1016/j.jhazmat.2019.121229.
[41] X.F. Li, T.X. Fan, Z.T. Liu, J. Ding, Q.X. Guo, D. Zhang, Synthesis and hierarchical pore structure of biomorphic manganese oxide derived from woods, J. Eur. Ceram. Soc., 26 (2006) 3657–3664.
[42] K.M. Parida, A.C. Pradhan, Removal of phenolic compounds from aqueous solutions by adsorption onto manganese nodule leached residue, J. Hazard. Mater., 173 (2010) 758–764.
[43] N. Zhang, G.M. Zhang, S. Chong, H. Zhao, T. Huang, J. Zhu, Ultrasonic impregnation of MnO_2/CeO_2 and its application in catalytic sono-degradation of methyl orange, J. Environ. Manage., 205 (2018) 134–141.
[44] H.Y. Liu, W.D. Zeng, A.L. Cao, C.Q. Zhang, Follicle-stimulating hormone promotes proliferation of cultured chicken ovarian germ cells through protein kinases A and C activation, J. Zhejiang Univ. Sci. B, 11 (2010) 952–957.
[45] H. Tamura, N. Katayama, R. Furuichi, The Co^{2+} adsorption properties of Al_2O_3, Fe_2O_3, Fe_2O_3, TiO_2, and MnO_2 evaluated by modeling with the Frumkin isotherm, J. Colloid Interface Sci., 195 (1997) 192–202.
[46] S.V. Mohan, N.C. Rao, J. Karthikeyan, Adsorptive removal of direct azo dye from aqueous phase onto coal based sorbents: a kinetic and mechanistic study, J. Hazard. Mater., 90 (2002) 189–204.
[47] Z.H. Liu, K. Ooi, H. Kanoh, W.P. Tang, T. Tomida, Synthesis of silica-pillared microporous manganese oxide, Chem. Lett., 29 (2000) 390–391.
[48] X.H. Tang, Z.H. Liu, C.X. Zhang, Z.P. Yang, Z.L. Wang, Synthesis and capacitive property of hierarchical hollow manganese oxide nanospheres with large specific surface area, J. Power Sources, 193 (2009) 939–943.
[49] S.A. Chaudhry, T.A. Khan, I. Ali, Adsorptive removal of Pb(II) and Zn(II) from water onto manganese oxide-coated sand: isotherm, thermodynamic and kinetic studies, Egypt. J. Basic Appl. Sci., 3 (2019) 287–300.
[50] W.H. Zou, R.P. Han, Z.Z. Chen, J.H. Zhang, J. Shi, Kinetic study of adsorption of Cu(II) and Pb(II) from aqueous solutions using manganese oxide coated zeolite in batch mode, Colloid Surf., A, 279 (2006) 238–246.
[51] L.Y. Jiang, L. Liu, S.D. Xiao, J.M. Chen, Preparation of a novel manganese oxide-modified diatomite and its aniline removal mechanism from solution, Chem. Eng. J., 284 (2016) 609–619.
[52] I.A. Katsoyiannis, A.I. Zouboulis, Biological treatment of Mn(II) and Fe(II) containing groundwater: kinetic considerations and product characterization, Water Res., 38 (2004) 1922–1932.
[53] R.P. Han, W.H. Zou, Z.P. Zhang, J. Shi, J.J. Yang, Removal of copper(II) and lead(II) from aqueous solution by manganese oxide coated sand - I. Characterization and kinetic study, J. Hazard. Mater., 137 (2006) 384–395.
[54] C.M. Xiong, W. Wang, F.T. Tan, F. Luo, J.G. Chen, X.L. Qiao, Investigation on the efficiency and mechanism of Cd(II) and Pb(II) removal from aqueous solutions using MgO nanoparticles, J. Hazard. Mater., 299 (2015) 664–674.